Ferrous hydroxychlorides hibbingite (γ-$Fe_2(OH)_3Cl$) and parahibbingite (β-$Fe_2(OH)_3Cl$) as a concealed sink of Cl and H_2O in ultrabasic and granitic systems

Revision 2

Word Count: 10513 (excluding tables)

Peter Koděra[1]*, Juraj Majzlan[2], Kilian Pollok[2], Stefan Kiefer[2], František Šimko[3], Eva Scholtzová[3], Jarmila Luptáková[4] and Grant Cawthorn[5]

[1]Department of Mineralogy, Petrology and Economic Geology, Faculty of Natural Sciences, Comenius University, Ilkovičova 6, 842 15 Bratislava, Slovakia

[2]Institut für Geowissenschaften, Mineralogie, Friedrich-Schiller-Universität Jena, Carl-Zeiss-Promenade 10, D-07745 Jena, Germany

[3]Institute of Inorganic Chemistry, Slovak Academy of Sciences, Dúbravská cesta 9, 845 36 Bratislava, Slovakia

[4]Earth Science Institute, Slovak Academy of Sciences, Ďumbierska 1, 974 01, Banská Bystrica, Slovakia

[5]School of Geosciences, University of the Witwatersrand, PO Wits, Johannesburg, South Africa

*E-mail: kodera1@uniba.sk

Abstract

Ferrous hydroxychlorides are geochemically important, but less recognized, mineral species due to their extreme sensitivity to oxidation and hydration in contact with air (typically they convert to

akaganéite [Fe^{3+}(O,OH,Cl)]). Only the γ-form was previously known as the orthorhombic mineral hibbingite, associated with altered mafic intrusive rocks. In this study, we describe the β-polymorph of $Fe_2(OH)_3Cl$ as a new mineral parahibbingite that was found in pyroxenite from the Karee platinum mine in the Bushveld Complex, South Africa. The two minerals were distinguished by a combination of Raman spectroscopy and FIB-SEM-TEM analytical techniques (TEM-EDX and TEM-SAED). They can be easily recognized by their distinct Raman spectra. Parahibbingite has two very strong vibration bands at ~3550 and 3560 cm^{-1}, accompanied by much weaker bands at ~124 and 160 cm^{-1} while the Raman spectrum of hibbingite has a sharp strong band at 3450 cm^{-1} and two moderate bands at 199 and 385 cm^{-1}.

Parahibbingite was found as fine-grained reaction rims on the contact of orthopyroxene phenocrysts and talc, inside a drill core. It is trigonal (space group $R\bar{3}m$, a=6.94(5) Å; c=14.5(2) Å), with an empirical formula $(Fe^{2+}_{1.98}Mn^{2+}_{0.01}Ca_{0.01})(OH)_{3.08}Cl_{0.92}$. The origin of this mineral in the Bushveld Complex is most likely related to a late hydrothermal alteration of pyroxenite. Hibbingite forms as an abundant daughter mineral hosted by fluid inclusions and salt melt inclusions in hydrothermal quartz associated with granitic systems during cooling under reducing conditions. Such inclusions are common in Au-porphyry mineralization worldwide, such as the deposit Biely Vrch (Slovakia) studied in detail in this work. The lattice parameters obtained by TEM-SAED are a=6.30 Å, b=7.12 Å, c=9.89 Å.

Hibbingite was recognized as the only phase that carries "water" (as a hydroxyl group) in otherwise water-free salt melt inclusions. Furthermore, both minerals should be considered as reservoirs for Cl and H_2O in large volumes of altered basic and ultrabasic rocks. They can transport volatiles into shallow levels of subduction zones. Alternatively, their dissolution can fuel remobilization, transport, and deposition of sulfidic ores in saline fluids. Their detection, however, is

difficult, because of their sensitivity to oxidizing atmospheres. For example in natural outcrops exposed to air, they may vanish, thus distorting estimates of their abundance and role in many processes that involve mineral-derived volatiles.

Keywords: ferrous hydroxychloride, Raman, parahibbingite, hydrothermal alteration, fluid inclusion

Introduction

Ferrous hydroxychloride is a chemical compound that can crystallize as three polymorphs: α, β and γ (Oswald and Feitknecht 1964). All three polymorphs of $Fe_2(OH)_3Cl$ are structurally well characterized, however, their affiliation to a particular form of $Fe_2(OH)_3Cl$ has rarely been examined in geological materials, and only the γ-form has been described as the mineral hibbingite (Saini-Eidukat et al. 1994). The α-form is metastable, thus it is less likely to occur in nature over geological periods of time, but the β-form has been known for a relatively long time in archaeological and corrosion sciences as the product of corrosion of man-made iron objects (e.g. Neff et al. 2005; Réguer et al. 2015). However, β-$Fe_2(OH)_3Cl$ was never determined in geological samples, except from iron meteorites (e.g., Buchwald and Koch 1995). This can be ascribed to the fact that all forms of $Fe_2(OH)_3Cl$ are extremely liable to oxidation and hydration and therefore very difficult to identify by conventional methods, especially if the grains are of small size. Therefore, it is possible that the β-form of $Fe_2(OH)_3Cl$ remained unrecognized even in those localities in the world where the presence of a mineral with hibbingite-like chemistry was already described, but with the lack of structural data it was just declared as hibbingite. There are several studies that describe the mineral hibbingite in various localities, but only two of them can be unequivocally ascribed to the γ-form of $Fe_2(OH)_3Cl$ (the "true" hibbingite), based on the evidence from X-ray diffraction analyses. Both of them are

associated with mafic intrusive rocks and PGE mineralisation (Duluth Complex - Saini-Eidukat et al. 1994; Noril'sk district - Zubkova et al. 2019). Hibbingite was also suggested, but never proven, to occur in similar rocks in other localities worldwide (e.g., Springer 1989, Cawthorn et al. 2009), but also in the form of daughter minerals in high-salinity fluid inclusions and salt melt inclusions from magmatic hydrothermal systems (e.g., Campos et al. 2002, Koděra et al. 2004, 2010, 2015, Kurosawa et al. 2016).

Recently, Réguer et al. (2015) proposed that the β-form of $Fe_2(OH)_3Cl$ is suspected to occur in natural samples, such as serpentinized mafic rocks, in addition to the γ-form. In our work, the mineralogical form of β-$Fe_2(OH)_3Cl$ was confirmed at chemical, atomic and molecular levels in a sample from the Bushveld Complex and described as a new mineral parahibbingite. We also provide a comparative study of ferrous hydroxychlorides that occur in rocks, brine inclusions, and salt-melt inclusions using a combination of methods, including Raman spectroscopy that can be used for rapid and reliable distinction of the various polymorphs of the ferrous hydroxychlorides. The presence of such phases can be suspected in many environments, such as altered ultrabasic rocks, high-temperature magmatic fluids related to intermediate magmatism, or in archaeological artefacts. In the former two, they could play an important but yet unrecognized role as vehicles for H_2O and Cl into the lower crust and lithospheric mantle, or, during their decomposition, as a source of volatiles for fluids that leach metals from the host rocks. Furthermore, hibbingite is recognized as the only phase that stores water in the form of the hydroxyl group in otherwise water-free salt melt inclusions.

In order to unequivocally confirm the identification of hibbingite and other possible polymorphs of $Fe_2(OH)_3Cl$, a detailed mineralogical study was performed on two samples: a sample hosting $Fe_2(OH)_3Cl$ in a mafic intrusive rock from the Karee Pt mine in the Bushveld Complex, South Africa and a sample with salt melt inclusions from the Biely Vrch porphyry gold deposit, Slovakia.

$Fe_2(OH)_3Cl$ polymorphs

The ideal composition of $Fe_2(OH)_3Cl$ requires Fe 56.36 %, Cl 17.89 %, H 1.53 %, and O 24.22 %. It can crystallize in three polymorphs:

- *α-form*, which crystallizes in the hexagonal system with brucite type structure (β-$Mg(OH)_2$) and the space group *P3m1* (Oswald and Feitknecht 1964). However, this is a metastable transient phase that is thought to occur during the crystallization of the stable β-form.

- *β-form*, new mineral parahibbingite (recently approved by the International Mineralogical Association; IMA2020-038a), crystallizes in the trigonal system with the space group $R\bar{3}m$ (Oswald and Feitknecht 1964, Réguer et al. 2015), and is isostructural with β-$Co_2(OH)_3Cl$ (de Wolff 1953).

- *γ-form*, which is known as the mineral hibbingite, is a member of the atacamite group. It crystallizes in the orthorhombic system with the space group *Pnma* (Saini-Eidukat et al. 1994, Zubkova et al. 2019).

Natural examples of $Fe_2(OH)_3Cl$

$Fe_2(OH)_3Cl$ in rocks

The first record of a ferrous hydroxychloride in rocks was by Springer (1989), who recognized this phase in samples from the Strathcona Deep Copper Zone on the northern rim of the Sudbury basin utilizing electron microprobe analyses. The $Fe_2(OH)_3Cl$ phase occurs in fracture fillings in chalcopyrite and pentlandite and converts upon exposure to air to akaganéite (*β*-FeOOH).

Hibbingite, as a new mineral, was first described in rocks of the Duluth Complex, Minnesota, USA (Dahlberg and Saini-Eidukat 1991, Saini-Eidukat et al. 1994), where it is associated with minor

PGE mineralization. It occurs most often as vein fillings in partially serpentinized troctolitic rocks. The hibbingite veinlets crosscut olivine or plagioclase grains or occur along grain boundaries or cleavage planes, as for example in biotite. It is accompanied by secondary magnetite or goethite and exhibits feathery intergrowth textures with serpentine minerals. The mineral is slightly pleochroic and colorless to pale green when unoxidized but becomes increasingly reddish with oxidation, has a grain size up to 700 μm, contains ~1.5 wt% Mn, and is soluble in H_2O.

Hibbingite from the Oktyabrsky Cu–Ni–Pd–Pt mine in the Noril'sk district, Russian Federation is a late-stage hydrothermal mineral, which occurs as transparent pale greenish crystals up to 2 mm in size. The grains fill vugs in massive sulfide ore that consist mainly of chalcopyrite, pentlandite [$(Ni,Fe)_9S_8$], cubanite ($CuFe_2S_3$), and mooihoekite ($Cu_9Fe_6S_{16}$) (Zubkova et al. 2019). Hibbingite contains minor Mn (1.8 wt%). If exposed to air, hibbingite was observed to alter to brown earthy aggregates of goethite and amorphous Fe(III) oxide-hydroxides. Hibbingite from Noril'sk was also described by Saini-Eidukat et al. (1998) as grains up to 0.6 mm in diameter associated with platinum-group minerals and native silver in a massive sulfide ore. Some hibbingite samples from Noril'sk contained a significant kempite ($Mn_2(OH)_3Cl$) component (17 to 50 wt. % Mn).

Saini-Eidukat et al. (1998) described hibbingite from the Korshunovskoye iron deposit in the southern Siberian platform, Russian Federation. It was found here in the form of grains up to 100 μm in length or encrustations in halite cavities and it contained just ~0.1% Mn. The halite acts as a cement for the fine-grained magnetite ore. The halite cavities also contain hematite and silver grains.

Hibbingite was also tentatively identified in exploration boreholes at the Karee platinum mine of the western Bushveld Complex, South Africa, based on its petrographic features and qualitative electron-microprobe analysis (Cawthorn et al. 2009). It occurs as veins 0.1 mm thick that cut serpentine veins in olivine grains.

The presence of hibbingite is also mentioned by Mikhailenko et al. (2016) from the Uduchnaya pipe salty kimberlites, Siberia, Russian Federation as a part of hydrothermal alteration mineral assemblage, together with serpentinite, halite, calcite, iowaite [$Mg_6Fe_2(OH)_{16}Cl_2.4H_2O$], barite, and celestine.

Lastly, the β-form of $Fe_2(OH)_3Cl$ has been described as a product of terrestrial weathering in iron meteorites, where it occurs as thin films and as up to 1 × 0.1 mm veins and void fillings often associated with akaganéite [$Fe^{3+}(O,OH,Cl)$] (Buchwald 1989, Buchwald and Koch 1995, Lee and Bland 2004).

$Fe_2(OH)_3Cl$ in fluid inclusions

In fluid inclusions, the possible occurrence of a ferrous hydroxychloride daughter mineral was for the first time proposed by Farrow et al. (1994), who analyzed the minerals from opened brine inclusions in chalcopyrite from the Sudbury Cu-Ni-PGE deposits in Canada by quantitative SEM-EDS analyses. These inclusions also contained halite and $BaCl_2$. Campos et al. (2002) suggested the presence of hibbingite in multi-solid fluid inclusions hosted by quartz phenocrysts from the Zaldívar Cu-porphyry deposit, northern Chile. The inclusions also contained halite, sylvite and some tiny opaque phases. The identification was based on the proton induced X-ray emission (PIXE) analysis that indicated a prevalence of Fe over Mn and Cu. The hibbingite-like mineral was semitransparent, typically showing a greenish-blue color and strong birefringence. On heating, it dissolved between 100 and 160 °C.

Koděra et al. (2003, 2004) suggested the presence of hibbingite in high-salinity brine inclusions from biotitized granodiorite with endoskarn alteration from the Fe-skarn deposit in Vyhne-Klokoč, Slovakia (Table 1; Fig. 1a). The inclusions were hosted by magmatic quartz and contained

several daughter minerals, including halite, sylvite, various K-Fe^{2+}-Cl hydrates and pyrosmalite-(Fe) [$Fe_8^{2+}Si_6O_{15}(OH,Cl)_{10}$]. The presence of hibbingite was deduced from the combination of SEM-EDS analyses of opened inclusions and Raman spectroscopy. SEM-EDS showed the presence of Fe-Cl and Fe-K-Cl-bearing solids (Koděra et al. 1998), while the Raman spectra of one of the solids provided a sharp strong peak at 3450 cm^{-1}, which is indicative of the presence of OH group in the structure of the mineral (Koděra et al. 2003). The spectra also included two moderately strong peaks at 199 and 385 cm^{-1} (Table 1, Fig. 1a). The hibbingite had a green-yellow color and a high relief. On heating, it dissolved in the range from 324 to 465 °C.

The same Raman spectra were later obtained from a daughter mineral of green color, hosted by brine inclusions in an early quartz veinlet at the Vysoká-Zlatno Cu-Au skarn-porphyry deposit in Slovakia (Koděra et al. 2010; Table 1; Fig. 1b). The veinlet was present in a granodiorite porphyry intrusion affected by K- and Ca-Na alteration. The inclusions always included halite, sylvite, and various Fe-K-Cl bearing phases, including $FeCl_2 \cdot 4H_2O$. On heating, all Fe±K-Cl phases dissolved below 150 °C.

Very similar Raman spectra were also determined for the daughter minerals in brine inclusions in quartz from the Chorloque Sn-porphyry, Bolivia and in Sn-W-Fe veins related to the Dartmoor granite, United Kingdom (Koděra et al. 2003; Table 1; Fig. 1c-d). The Chorloque inclusions also hosted halite, rokühnite ($FeCl_2 \cdot 2H_2O$) and an unknown Fe-K-Cl hydrate. The Dartmoore inclusion contained halite and some other unidentified phases.

Recently, nearly identical Raman spectra were also determined from a daughter mineral in polyphase inclusions in quartz from a miarolitic cavity and quartz veins in the Tsushima granite, Japan, which is genetically related to the adjacent Pb-Zn vein-type Taishu Mine deposit (Kurosawa et al. 2016). The analyzed polyhedral crystals were colorless to pale green, anisotropic, and occupied up to about 10% of the inclusion volume. The inclusions also contained halite, sylvite, $FeCl_2 \cdot 4H_2O$,

rokühnite ($FeCl_2.2H_2O$), saltonseaite ($K_3NaMnCl_6$), pyrosmalite-(Fe) [$Fe_8Si_6O_{15}(OH,Cl)_{10}$] and siderite. On heating, all phases, except halite, disappeared at temperatures below 150 °C.

In summary, even though the presence of ferrous hydroxychlorides in Fe-rich brine inclusions has been documented for a series of localities in the world, and all the phases share the same distinct type of Raman spectrum (Table 1; Fig. 1), it has never been determined which of the polymorphs of $Fe_2(OH)_3Cl$ it belongs to.

$Fe_2(OH)_3Cl$ in salt melt inclusions

A hibbingite-like phase was also determined as an abundant daughter mineral hosted by salt melt, liquid-free inclusions that occur in several porphyry gold systems in the Central Slovak Volcanic Field (Koděra et al. 2017, Kozák et al. 2017). Salt melt inclusions represent a rare type of fluid inclusion, where the entire volume of the inclusion is occupied by several salt crystals and a distorted vapor bubble (Koděra et al. 2014). The inclusions contain commonly a greenish or pale green-yellowish phase of a tabular habit whose Raman spectrum corresponds to the spectra of the hibbingite-like mineral in brine inclusions, presented above. The diagnostic Raman spectrum of the hibbingite-like mineral was determined in salt melt inclusions from four different localities in two stratovolcanoes: Biely Vrch, Králová and Slatinské Lazy in the Javorie stratovolcano, Slovakia (Koděra et al. 2017), as well as Beluj in the Štiavnica stratovolcano, Slovakia (Kozák et al. 2017 and this study; Table 1; Fig. 1e-i). On heating of the inclusions, the mineral melted in the range of 350 to 450 °C. Salt melt inclusions from all localities are predominantly hosted by granular vein quartz, resembling the A-veinlets of Gustafson and Hunt (1975) and rarely by pyroxene veinlets. The most common accompanying salt crystals are halite, javorieite ($KFeCl_3$), chlorocalcite ($KCaCl_3$) and rinneite ($K_3NaFeCl_6$) that were identified by a combined Raman, FIB-EDS, FIB-EBSD and microthermometric study (Koděra et al. 2015, 2017).

$Fe_2(OH)_3Cl$ in corrosion products

The β-form of $Fe_2(OH)_3Cl$ is already well known in the corrosion of man-made iron objects in archaeological artefacts. It occurs in those environments where low-carbon steel interacts with chloride-rich anoxic brines and forms thin corrosion layers, followed by outer layers of akagenéite and magnetite, and sometimes siderite (Buchwald 1989, Neff et al. 2005, Réguer et al. 2005, 2007, Nemer et al. 2011, Rémazeilles et al. 2009). Specifically, in iron objects corroded in marine environments, the β-form of $Fe_2(OH)_3Cl$ is the predominant corrosion product that can reach several millimeters in thickness (Rémazeilles et al. 2009). In this setting, it was also found to be accompanied by the minor γ-form of $Fe_2(OH)_3Cl$ (Réguer et al. 2015). Oxidation of the corrosion products results in the formation of akaganéite (*β*-form of FeOOH), which always contains some chloride (or fluoride) ions (Rémazeilles and Refait 2008).

Geological setting

Alteration products from the Bushveld Complex

The Bushveld Complex outcrops in the northern part of South Africa and includes the largest layered intrusion on Earth - the Rustenburg Layered Suite (RLS). This layered series consists of a number of zones and contains globally the largest resources and reserves of platinum-group elements, located within the Merensky Reef, Platreef and the Upper Group 2 layer (UG2) (Godel 2015).

The samples with $Fe_2(OH)_3Cl$ come from exploration drill holes in the Karee platinum mine in the Rustenburg district that is located on the UG2 layer in the Critical Zone, stratigraphically below

the adjacent Merensky Reef (Appendix 1). Samples were provided by R.G. Cawthorn, who took a number of fresh and altered samples (10 cm of half core) from several drill cores in 2004. The presence of hibbingite in the drill cores was suspected to be due to the acidic coating that rapidly developed on the surface of the cores (Cawthorn et al. 2009). In the initial study, (Cawthorn et al. 2009), the material was cut and crushed, but all pieces were then stored in plastic bags. When sampling for the current study, further alteration of the rocks was noticed, especially of the olivine-bearing samples. Three larger samples showing least surface alteration were selected, but only one of them was recognized to contain a hibbingite-like mineral. Unfortunately, the position of this sample in the original sequence of cores is not exactly known, but it was chosen because it was by far the largest piece of an intact core remaining, and hence considered likely to yield the best material for study. This sample is a pyroxenite that comes from the immediate vicinity of the UG2 chromitite (footwall or hanging-wall, unreported). A hibbingite-like mineral was found to be relatively common and still mostly unaltered, but always present just in the unoxidized, inner part of sample.

Salt melt inclusions from the Biely Vrch deposit

The Biely Vrch porphyry gold deposit occurs in the central zone of the Javorie stratovolcano, which is a part of the Middle Miocene, Central Slovak Volcanic Field, Slovakia. This field is situated on the inner side of the Carpathian arc and consists of several large andesitic stratovolcanoes (Konečný et al. 1998). Porphyry gold mineralisation was recently discovered here at more than ten localities in two major stratovolcanoes (Javorie and Štiavnica; Appendix 2). All were hosted by stocks of diorite porphyries emplaced in andesites and prevolcanic basement rocks (Hanes et al. 2010, Bakos et al. 2010, Koděra et al. 2014). The Biely Vrch deposit in the Javorie stratovolcano is the biggest and best explored locality. It represents an economic accumulation of gold ore (27 Mt at 0.85 g/t Au; AMC, 2010).

The salt melt inclusions at Biely Vrch, as well as at other localities, coexist with abundant vapour-rich fluid inclusions. They contain a distorted vapor bubble and several salt crystals, including hibbingite, which was tentatively identified based on a distinct Raman spectrum (Fig. 1e-i). In this study, a detailed study of hibbingite has been performed on a sample from a porous quartz vein at Biely Vrch obtained via an inclined drill hole DVE-51 at a depth of 475 m along the hole.

Methods

The mafic intrusive pyroxenite from the Karee mine (sample K-37-19), was initially studied as two polished sections that were prepared without the use of water in order to avoid oxidation and hydration of the ferrous hydroxychlorides, suspected to occur in the rock. Salt melt inclusions hosted in vein quartz from the Biely Vrch deposit were studied in doubly polished wafers (~200 μm thick), prepared in the usual way.

The polished sections from Karee were investigated by back-scattered electron imaging, semi-quantitative (EDS) and quantitative electron microprobe (EMP) analyses using the CAMECA SX-100 electron microprobe at the State Geological Institute, Dionýz Štúr, Bratislava, Slovakia and using a JEOL JXA 8230 electron microprobe at the Institut für Geowissenschaften, Jena, Germany. Conditions for the hibbingite EMP analyses were as follows: acceleration voltage 15 kV; beam current 20 nA, beam diameter 5 μm. The water content was calculated from stoichiometry to charge balance the chemical formula. The standards and analytical lines selected were as follows (Bratislava/Jena): fayalite/hematite (Fe Kα), rhodonite (Mn Kα), forsterite/MgO (Mg Kα), wollastonite (Si Kα, Ca Kα), Al_2O_3 (Al Kα), albite (Na Kα), orthoclase (K Kα), TiO_2 (Ti Kα), NaCl (Cl Kα), LiF (F Kα), chromite (Cr Kα), Ni (Ni Kα).

Raman scattering of $Fe_2(OH)_3Cl$ grains from Karee, located by SEM imaging and identified by EDS and EMP analyses, was investigated next day. However, the surface of thin sections was first re-polished in order to remove the carbon coating, which was necessary for the EMP study. Raman analyses were performed by a Horiba Jobin-Yvon LabRam HR800 spectrometer, equipped with an Olympus BX41 optical microscope in the laboratory of Earth Science Institute of the Slovak Academy of Sciences in Banská Bystrica, Slovakia. Polarized laser emission at λ=532 nm (frequency-doubled Nd:YAG laser) was used for excitation. The Raman-scattered light was collected in 180° geometry through a 100x objective lens with a numerical aperture of 0.8 and dispersed by a diffraction grating with a density 600 grooves/mm onto a Peltier cooled CCD detector Synapse (Horiba Jobin-Yvon). Spectra were collected in two acquisitions of 30 seconds in the range 70-4000 cm^{-1}. The bands from a teflon standard were used to calibrate the spectrometer. The same instrument and analytical setting were also used for Raman spectroscopy of daughter minerals in salt melt inclusions hosted in vein quartz in a drill core from the Biely Vrch deposit. The vibrational spectrum of a pure γ-$Fe_2(OH)_3Cl$ (hibbingite) was further investigated using the Density Functional Theory (DFT), including calculation of optimized cell parameters and total vibrational bands of this compound. Details of the calculations are presented in Appendix 3.

In order to determine the structural form of $Fe_2(OH)_3Cl$ in hibbingite-like minerals, we used transmission electron microscopy (TEM) on focused ion beam (FIB) prepared sections (Institute for Geosciences, Friedrich Schiller University Jena). This combination ensures that the sample has a minimum contact with air as preparation and analysis are performed in a high vacuum with a short transfer time (<5 minutes) between the instruments. Furthermore, it enables measurements of electron diffraction patterns of the same phases that were previously analyzed by EMP and/or in-situ Raman analyses. FIB preparation was conducted using a FEI Quanta 3D FEG FIB-SEM instrument that

enabled a progressive abrasion of the targeted area in the mineral using a focused beam of Ga ions, monitored by SE and BSE imaging. The Ga ion gun was operated at 30 kV with a beam current between 30 to 0.1 nA for sample preparation. A deposited Pt stripe was used to protect the surface. To remove amorphous layers on the FIB cut (which form during the preparation), the foils were cleaned at 5 kV using 48 pA beam current. TEM on the mineral foil was performed with a FEI Technai G^2 FEG TEM, operating at 200 keV using a double tilt holder. TEM images were taken by a 2K CCD camera (Gatan Ultrascan). The UnitCell program (Holland and Redfern 1997) was used for the refinement of the lattice constants using *d* values obtained from 6 electron diffraction patterns on 4 different grains from the Bushveld Complex sample and from 2 diffraction patterns on a single crystal from the Biely Vrch sample. Powder X-ray diffraction data were reduced using the Diamond software, version 4. Parahibbingite crystal data are summarized in the Crystallographic Information File (CIF), available in the Supplemental material.

The chemical composition of hibbingite and other daughter minerals in salt melt inclusions were obtained by TEM-EDX point analyses, which were used on the same instrument along with the selected area diffraction (SAED) analyses. Point analyses using TEM are semiquantitative as they suffer from stray radiation, which produces a Cu signal from the Cu grid as well as signals from neighbouring phases of variable intensity.

Results

Identification and characteristics of parahibbingite from the Bushveld Complex

Petrographic observations and microanalytical study of the pyroxenite sample with the hibbingite-like mineral (Fig. 2; Appendix 7) showed that the host rock is composed predominantly of euhedral orthopyroxene ($En_{74-76}Fs_{23-24}Wo_{0-2}$) crystals up to 4 mm long, variably replaced by Fe-Mg-Mn amphibole (cummingtonite) and less frequently by Ca-amphiboles of variable composition

(magnesio-ferri-hornblende, actinolite, tremolite). No olivine was found. The latest alteration product is ferroan talc with a variable Fe content (7.1–13.1 wt% FeO) that partially replaces both the orthopyroxene and amphiboles, locally forming reaction rims accompanied by the hibbingite-like mineral. Minor plagioclase ($Ab_{50-53}An_{47-49}Or_{0-2}$), rare biotite, quartz, and Cr-rich spinel (39.0–41.0 wt.% Cr_2O_3) are also present in the early mineral assemblage.

The hibbingite-like mineral (hereafter called parahibbingite) occurs in talc that has partially or totally replaced orthopyroxene, typically in the form of rims or clusters mostly on the contact between orthopyroxene and talc (Fig. 2). The mineral forms fine-grained coatings, reaction rims, and aggregates hosted by talc, and short, tiny veinlets that are parallel to the cleavage of cummingtonite (Fig. 2e, 2f). Locally it is also associated with carbonates (siderite, dolomite, calcite), sulfides (pyrrhotite, pentlandite, chalcopyrite), clays (sericite), spinel-group minerals (chromite with a hercynite component) and Fe-Ti oxides (rutile, magnetite). The maximum size of individual aggregates of parahibbingite is up to 100 μm, but individual grains are usually smaller than a few microns in diameter.

In total, 56 EMP analyses of parahibbingite were performed (Table 2; Appendix 4), most of them approaching the chemical composition of hibbingite (Saini-Eidukat et al. 1994). However, several of them had low analytical totals or they contained a minor signal from the host talc (elevated Si and Mg contents). Some analyses show a minor but distinct excess of Cl^- (± F^-) compared to Fe^{2+}, which can be explained by the replacement of some hydroxyl groups by Cl. Variable Cl^-/OH^- ratio is described also for the α-$Fe_2(OH)_3Cl$ (Oswald and Feitknecht 1964). At least some of the variations in the analytical totals and analytical sums below 100% could be assigned to the fine-grained nature and porosity of the aggregates, visible already in the BSE images (Figs. 2 and 7). Table 2 shows the data from the 12 purest parahibbingite analyses with the highest total (~94–97 wt%) minus OH. No carbon

compound was identified by the Raman spectroscopy (see below) indicating that CO_2 is not present. Assuming charge balance, the empirical formula of parahibbingite was calculated from the three analyses with the highest total on the basis of 2 cations per formula unit assuming divalent Fe^{2+} and Mn^{2+}: $(Fe^{2+}_{1.98}Mn^{2+}_{0.01}Ca_{0.01})(OH)_{3.08}Cl_{0.92}$. The simplified formula is $(Fe,Mn,Ca)_2(OH)_3Cl$.

In one of the parahibbingite aggregates, three EMP analyses showed the presence of an additional unknown phase (see Appendix 5). This phase, only a few μm large, was intergrown with parahibbingite hosted in talc, and had a Fe^{2+}:OH:Cl ratio of about 1: 1: 1. Because of its minute size, it was not studied further.

Raman spectroscopy has shown that parahibbingite has two very strong vibration bands at around 3550 and 3560 cm^{-1}, accompanied by much weaker, but distinctive bands at around 124, 160, 317, 424, 614, and 816 cm^{-1} (Fig. 3, Table 3). In addition, the spectra always included Raman scattering of the host talc of variable intensity (Figs. 3 and 4). The Raman scattering bands correspond well to bands of β-$Fe_2(OH)_3Cl$ occurring as corrosion on archaeological artefacts (Réguer et al. 2007), as well as to bands of synthetic β-$Fe_2(OH)_3Cl$ (Rémazeilles and Refait 2008). Minor differences include the relative intensity of the first two peaks (124 and 160 cm^{-1}), which result from the crystallographic orientation of the grains (Fig. 3d). According to Réguer et al. (2007), the Raman scattering bands can be assigned to O-Fe-O bending mode (160 cm^{-1}), Fe-Cl, and Fe-O stretching vibrations (317, 424 cm^{-1}, and 613 cm^{-1}, respectively), hydroxyl deformation mode (816 cm^{-1}), and hydroxyl stretching vibrations (3550, 3561 cm^{-1}). Interestingly, a few of the Raman spectra also include a minor but distinctive sharp peak at about 3451 cm^{-1} (Fig. 4) that probably corresponds to the γ-form of $Fe_2(OH)_3Cl$ (hibbingite) (Fig. 1). Note that the minor presence of γ-$Fe_2(OH)_3Cl$ was also confirmed by FIB-TEM analyses (see below).

Electron diffraction of the TEM foil from β-$Fe_2(OH)_3Cl$ (parahibbingite) disclosed streaks, satellite, or superstructure reflections in several cases indicating that the crystallography of the mineral might be more complex due to the different connectivity of the iron octahedra in the structure. Furthermore, parahibbingite commonly shows a lamellar microstructure, which indicates either twinned areas or a structural perturbation (e.g., γ-$Fe_2(OH)_3Cl$ units within the β-$Fe_2(OH)_3Cl$ structure; Fig. 5). Most electron diffraction patterns indicate the presence of the β-form of $Fe_2(OH)_3Cl$ (Fig. 6a-c), however, some images could be indexed by the γ-form of $Fe_2(OH)_3Cl$ (Fig. 6d). The stability of the β phase under the electron beam was tested. It does not easily transform or dehydrate under electron irradiation. Therefore, the finding of areas with the γ structure appears to be intrinsic to the sample and not due to sample preparation or electron irradiation. Powder X-ray diffraction data for parahibbingite listed in Appendix 6 were calculated with the lattice parameters from this work and the structural model for β-$Co_2(OH)_3Cl$ (de Wolff 1953) as parahibbingite is assumed to be isostructural with β-$Co_2(OH)_3Cl$ (Oswald and Feitknecht 1964). The electron diffraction data from this work enabled the following lattice parameters to be determined: a = 6.94±0.05 Å; c = 14.5±0.2 Å; space group 166 ($R\bar{3}m$).

Due to the sensitive nature of the new mineral, most physical properties of parahibbingite could not be established on the type material, as only non-transparent polished sections could be prepared for this study. However, according to Rémazeilles and Refait (2008) synthetic β-$Fe_2(OH)_3Cl$ has a light-blue grey color, greyish streak, and vitreous luster. Under the microscope β-$Fe_2(OH)_3Cl$ is greenish (Buchwald and Koch 1995). The Gladstone-Dale relationship predicts an average index of refraction of 1.75. The mineral is extremely liable to oxidation. In contact with air, it converts to iron oxyhydroxides (typically akaganéite) just in a few hours. Larger grains can persist for a few days. On

the basis of empirical formula and unit cell volume refined from electron diffraction data, the calculated density of the mineral is 3.24 g/cm^{-3}.

Identification and characteristics of hibbingite from the Biely Vrch deposit

The studied sample of vein quartz from Biely Vrch contains numerous salt melt inclusions, each with several daughter minerals. Raman spectroscopy was used to recognize the mineral with the distinct spectrum that, according to the results presented below, can be attributed to the mineral hibbingite (Fig. 1). The most suitable inclusion in terms of a short distance to the surface of the wafer, which contained a sufficiently visible thick crystal of hibbingite was selected for FIB-TEM analytical work. The combination of Raman spectroscopy and FIB-SEM-TEM analytical techniques (TEM-EDX and TEM-SAED) proved that the inclusion overall contained halite, javorieite ($KFeCl_3$), rinneite ($K_3NaFeCl_6$), hibbingite, $BaCl_2$, and probably also chlorocalcite ($KCaCl_3$) (Fig. 7).

The chemical composition of the hibbingite crystal was studied via a series of EDX element maps that confirmed the presence of Fe, Cl, and O, which approximates the formula of hibbingite $(Fe)_2(OH)_3Cl$. The typical EDX point spectrum of hibbingite is shown in Figure 8 and three best EDX analyses are presented in Table 4. Most of the spectra showed elevated amounts of Na together with excess Cl, which most probably originates from the surrounding halite. For these analyses, Na and a stoichiometric amount of Cl was removed, and the analyses were renormalized thereafter. However, at least one analysis showed an almost ideal hibbingite composition (analysis 1 in Table 4). In this analysis, no NaCl signal was present and only a small absorption correction was applied.

Electron diffraction data were obtained from 3 zone axes [0-1-1], [1-1-1] and [2-1-1] (Fig. 9, Table 5), which allowed for the following lattice parameters to be determined: a = 6.30 Å, b = 7.12 Å,

c = 9.89 Å, which are clearly different to those from parahibbingite (β-$Fe_2(OH)_3Cl$) presented above but are similar to those published for hibbingite (Saini-Eidukat et al. 1994, Zubkova et al. 2019).

As presented above, the Raman spectrum of the hibbingite from fluid and salt melt inclusions from Biely Vrch and other localities worldwide has a sharp strong band at 3449 to 3451 cm^{-1}, two moderately strong bands at 198 to 199 cm^{-1} and 385 to 386 cm^{-1}, and a number of other small bands (Table 1). The assignment of the bands is likely similar to that for parahibbingite, described above. In order to further confirm the affiliation of this spectrum to hibbingite, DFT calculations were carried out, and the vibrational spectrum was calculated (Appendix 3). The calculations indicate the position of the Raman hydroxyl stretching vibrations of γ-$Fe_2(OH)_3Cl$ below 3500 cm^{-1}, in contrast to parahibbingite and all other ferrous hydroxide compounds.

Discussion

Structural aspects and classification

The obtained structural parameters of parahibbingite from the Karee mine were compared to the published structural data of β-$Fe_2(OH)_3Cl$ (Oswald and Feitknecht 1964, Réguer et al. 2015) and carefully distinguished from the related structure of the γ-$Fe_2(OH)_3Cl$ phase. Réguer et al. (2015) performed both X-ray absorption (XANES, EXAFS) and X-ray diffraction (XRD) studies on β-$Fe_2(OH)_3Cl$. They used the XANES and EXAFS data together with the XRD results to produce the best refinement of the structure (i.e., XANES and EXAFS for Fe and Cl local environments; XRD for the long-range structure). Their refined structural parameters are in a very good agreement with those obtained in this study (Table 6). The observed variation in the d spacing from grain to grain of parahibbingite could be due to locally variable OH/Cl^-ratios, due to the noted structural complexities, as well as due to temperature changes under the electron beam that may affect bond lengths in weakly

bonded phases. However, the geometry of electron diffraction patterns always matches the symmetry of the trigonal β-$Fe_2(OH)_3Cl$.

The structural parameters determined from electron diffraction data of hibbingite from salt melt inclusion from the Biely Vrch deposit match with those calculated for hibbingite by Saini-Eidukat et al. (1994), and to the refined single crystal X-ray diffraction data obtained by Zubkova et al. (2019) (Table 6). Electron diffraction patterns show additional spots which cannot be clearly assigned to hibbingite. This observation may point at local structural variations, such as domains of the β polymorph or compositional variations.

In this work, we have demonstrated that both forms of $Fe_2(OH)_3Cl$ can be present in one sample, while one of the forms [β-$Fe_2(OH)_3Cl$] is predominant. A similar observation was made by Rémazeilles et al. (2009) in iron archaeological artefacts excavated from seawater that were affected by long-term anaerobic corrosion. In their μXRD spectra, they have determined small peaks of γ-$Fe_2(OH)_3Cl$ along with the predominant (> 90 %) β-$Fe_2(OH)_3Cl$ (Réguer et al. 2015).

Hibbingite and parahibbingite belong to the transition metal hydroxyhalogenide series $M_2(OH)_3Cl$, where M represents a transition-metal d-electron magnetic ion such as Cu^{2+}, Fe^{2+}, Mn^{2+}, Co^{2+}, Ni^{2+}, and Cl^- is the halogen ion (Réguer et al. 2015). In the Strunz and Nickel classification system both polymorphs belong to the 3.DA class (Oxyhalides, Hydroxyhalides and Related Double Halides with Cu, etc., without Pb). In the New Dana classification, hibbingite belongs to the 10.01 class (Oxyhalides and Hydroxyhalides as $A_2(O,OH)_3X_q$) and in the 10.01.01 Atacamite group, which includes atacamite $Cu_2Cl(OH)_3$, that has unit-cell parameters similar to that of hibbingite. Hibbingite possibly forms a solid-solution series with kempite $Mn_2Cl(OH)_3$ (Saini-Eidukat et al. 1998). However, in our study the hibbingite does not contain any detectable kempite component. The new mineral parahibbingite belongs to the 10.1.1.2 Paratacamite group which includes paratacamite

$(Cu,Zn)_2(OH)_3Cl$, clinoatacamite $Cu_2(OH)_3Cl$, as well as herbertsmithite $Cu_3Zn(OH)_6Cl_2$, which is isostructural with parahibbingite (trigonal, space group $R\bar{3}m$).

Comparison of selected properties of parahibbingite and hibbingite is shown in Table 7. The structures of both minerals are sufficiently different to produce distinctly different Raman spectra, presented above, that enable an easy and quick recognition of these minerals in future studies. Furthermore, infrared spectroscopy can be also used for identification of the two minerals, although their IR spectra are quite similar. The IR spectrum of hibbingite shows a strong band at about 3552 cm^{-1} due to the OH stretching vibration (Saini-Eidukat et al. 1994), whereas in the IR spectrum of synthetic β-$Fe_2(OH)_3Cl$ this band is located at 3555 cm^{-1} (Rémazeilles and Refait 2008). Other bands in the IR spectrum of synthetic β-$Fe_2(OH)_3Cl$ were found at 804 and 690 cm^{-1}, while the last band is asymmetric and may be composed of two peaks.

Relationships among the $Fe_2(OH)_3Cl$ polymorphs

Crystallization of the $Fe_2(OH)_3Cl$ polymorphs in geological environments requires involvement of saline fluids. Hibbingite usually forms by direct crystallization from the fluids in opened spaces, such as fillings of veins and cavities, including fluid inclusions and salt melt inclusions. In contrast, β-$Fe_2(OH)_3Cl$ (parahibbingite) always occurs as a replacement product – either at the expense of rock-forming silicates with Fe^{2+} (e.g., orthopyroxenes), iron meteorites, or man-made iron objects if they were in contact with chloride-rich anoxic brines.

The origin of parahibbingite and hibbingite in these samples is not entirely clear, and neither are the conditions that would trigger crystallization of a particular polymorphic modification of $Fe_2(OH)_3Cl$. The origin of parahibbingite in the sample from the Bushveld Complex is most likely related to a late hydrothermal alteration of the pyroxenite. Orthopyroxene phenocrysts are extensively

replaced by cummingtonite and talc, while parahibbingite often forms reaction rims on the contact of orthopyroxene and talc (Fig. 2). This textural position of parahibbingite indicates that it has crystallized simultaneously or shortly after the replacement of orthopyroxene by talc, but probably at lower temperatures compared to the origin of cummingtonite and other amphiboles. The formation of amphiboles represents an earlier, higher-temperature process of hydrothermal alteration. In these samples, talc has a significantly lower Fe/Mg ratio and FeO content compared to orthopyroxene or cummingtonite (Appendix 7), so the excess Fe^{2+} could have reacted with Cl^- in the hydrothermal fluids initiating crystallization of parahibbingite on the reaction front. Interestingly, talc locally also hosts sulfide minerals, which indicates that the formation of parahibbingite is related to hydrothermal processes responsible also for some hydrothermal sulfide mineralization.

The crystallization of hibbingite in salt melt and fluid inclusions is probably related to hot, high-salinity fluids of magmatic origin in acidic to intermediate magmatic systems. Based on the limited inclusions microthermometry data, summarized above, hibbingite crystallizes on cooling from ~460 to <150°C. According to Zubkova et al. (2019), crystallization of this mineral is only possible under strongly reducing conditions and thus the presence of this mineral in inclusions can be used as a good geochemical indicator showing low oxygen fugacity in a mineral-forming system.

As the relationship between β- (trigonal parahibbingite) and γ- (orthorombic hibbingite) ($Fe_2(OH)_3Cl$) is very close to that found for trigonal paratacamite and orthorombic atacamite (Fleet 1975, Kubozono et al. 2006, Zubkova et al. 2019), these well-studied Cu hydroxychloride minerals can be used as a rough analogue to evaluate the genetic relationship between the two ferrous hydroxychloride polymorphs. Copper hydroxychloride minerals occur in three polymorphic crystal forms: orthorhombic atacamite, monoclinic clinoatacamite, and monoclinic botallackite. Also known is trigonal paratacamite $(Cu,Zn)_2(OH)_3Cl$ which was regarded as an another $Cu_2(OH)_3Cl$ polymorph

in the past (Oswald and Guenter 1971, Pollard et al. 1989). All these polymorphs occur as secondary minerals in areas of Cu mineralization and as corrosion products of bronze and Cu objects of antiquity (Jambor et al. 1996). Atacamite is the most common polymorph, found especially in arid, saline conditions, where it commonly coexists with clinoatacamite and paratacamite. Botallackite is of limited natural occurrence, but it crystallizes first under most conditions (Pollard et al. 1989). It is metastable and it recrystallizes quickly to more stable $Cu_2(OH)_3Cl$ polymorphs and thus it might only be preserved if solutions responsible for its crystallization are quickly dried out. Clinoatacamite is the thermodynamically most stable phase at ambient temperatures. Thus, the crystallization in the $Cu_2(OH)_3Cl$ system follows the sequence botallackite → atacamite → clinoatacamite which corresponds to the Ostwald step rule (Krivovichev et al. 2017). The formation of paratacamite is enabled by the presence of substituting cations such as Zn or Ni, even though these may be as little as 2-4 wt.%. In the absence of these cations, the mineral more likely to form is clinoatacamite rather than paratacamite (Jambor et al. 1996). In addition, there exist another related secondary Cu mineral belloite Cu(OH)Cl, that is known to be unstable in humid, non-desert environments, where it converts to botallackite and atacamite (Schlüter et al. 2000).

It is not known which of the $Fe_2(OH)_3Cl$ polymorphs is typically the first solid that crystallizes from a solution, but according to the Ostwalds step rule it should be the least stable polymorph. By analogy with the Cu hydroxychloride minerals it could be hibbingite. However, in high salinity fluid inclusions, hibbingite persists at ambient conditions for millions of years after crystallization at elevated temperatures. Therefore, the relationship between hibbingite and parahibbingite is not clear, but it is likely that parahibbingite recrystallizes from the former hibbingite precursor, as indicated by the rare presence of hibbingite fragments in parahibbingite. Alternatively, parahibbingite could have formed together with minor hibbingite by direct crystallization during brine/rock (or brine/metal) interaction. As hibbingite was also found in archaeological artifacts, it is clear that the presence of the

two polymorphs is not related to differences in temperature of origin. Furthermore, the possible presence of Fe(OH)Cl phase fragments, which likely is an analogue to belloite, hosted by parahibbingite grains, also suggests that parahibbingite is the most stable phase in the $Fe_2(OH)_3Cl$ system. However, further studies are needed to understand the relative stabilities of polymorphs in the ferrous hydroxychloride system.

Implications

Parahibbingite and hibbingite can play an important role in the storage of Cl in large volumes of hydrothermally altered ultramafic rocks, where the alteration was caused by reduced post-magmatic brines (Rucklidge and Patterson 1977), sea water penetrating into a newly formed oceanic crust, or fluids derived from dissolution of evaporite sediments (Saini-Eidukat et al. 1998, Vanhanen 2001). Under reducing and saline conditions, ferrous hydroxychlorides can form if the Mg/Fe ratio in alteration products is lower than that in the primary minerals. For example, Rucklidge and Patterson (1977) suggested the reaction

$$4(Mg_{0.75}Fe_{0.25})_2SiO_4 + 5H_2O + HCl = 2Mg_3Si_2O_5(OH)_4 + Fe_2(OH)_3Cl \qquad (1)$$

In this reaction, serpentine minerals form upon alteration of the primary olivine. Serpentine minerals themselves are known to store Cl in two forms (Sharp and Barnes 2004): i) weakly bound and ii) substituted for OH groups in their structure. Sheet silicates are known to adsorb ions onto their surfaces (Brown et al. 1999) but they have much greater affinity for cations because of their permanent negative surface charge. In addition, the serpentine minerals in serpentinite do not possess the large surface areas typical for sheet silicates in soils and sediments. Based on our observations and properties of sheet silicates, we propose that the weakly bound reservoir of Cl in altered ultramafic rocks could consist of hibbingite or parahibbingite.

In our samples, orthopyroxene is altered to talc and parahibbingite according to the reaction

$$8(Mg_{0.75}Fe_{0.25})SiO_3 + 3H_2O + HCl = 2Mg_3Si_4O_{10}(OH)_2 + Fe_2(OH)_3Cl \quad (2)$$

Both reactions should be common in nature but the ferrous hydroxychlorides or other chlorides (NaCl, $MgCl_2 \cdot 6H_2O$) were not observed in studies that attempted to find them (Anselmi et al. 2000; Bonifacie et al. 2008; Huang et al. 2017).

Hibbingite and parahibbingite can be formed during hydrothermal alteration or veining of ultramafic rocks and carry OH and Cl into subduction zones. Little is known about their stability at elevated temperature or pressure; the available thermodynamic data (Nemer et al. 2011) refer only to ambient conditions. It could be assumed that the stability of the $Fe_2(OH)_3Cl$ phases does not extend to high *P*-*T* conditions. They may be converted to Cl-bearing amphiboles that continuously supply H_2O and halogens into the mantle wedge during prograde metamorphism (Debret et al. 2016).

Alternatively, a further hydrothermal event could decompose or remobilize the ferrous hydroxychlorides allowing the released chloride to harvest and transport metals during the hydrothermal event. Thus, the crystallization of $Fe_2(OH)_3Cl$ minerals could be an important transitional event for later ore-remobilization and ore-forming processes. This is supported by the fact that remobilization of magmatic ore minerals by post-magmatic fluids is known and well documented in several large intrusive complexes, such as the Bushveld Complex (Ballhaus and Stumpfl 1986; Zhitova 2016; Kawohl and Frimmel 2016), the Duluth Complex (Mogessie and Stumpfl 1992; Ripley 1990; Dahlberg and Saini-Eidukat 1991), and the Sudbury Complex (Hanley and Mungall 2003). In each of these complexes, the presence of ferrous hydroxychlorides was also reported. A significant role of hibbingite in metals redistribution was also proposed by Vanhanen (2001) for the origin of Paleoproterozoic Fe-Co-Au-(U) deposits in the Kuusamo Schist Belt (NE Finland). The authors

assumed that hibbingite occurred there in pyrrhotite-rich sedimentary beds due to hydrothermal activity generated by mafic magmatism and the dissolution of halite from evaporites.

In this work, we have also shown that hibbingite is a common component in crystallized inclusions of molten salts in porphyry-gold systems. In most salt melt inclusions, all other daughter minerals are anhydrous, thus hibbingite is the only "water sink" in these liquid-free inclusions. Therefore, the identification of hibbingite in inclusions enables us to exactly calculate the amount of water that was originally dissolved in the salt melts. Such fluids with extremely high chlorinity are able to transport gold and some other metals very efficiently (Koděra et al. 2014, 2018). The information on the water content is an important variable for understanding accompanying magmatic-hydrothermal processes.

The minerals hibbingite and parahibbingite are difficult to detect because of their sensitivity to air. It is also possible that they are washed away during standard sample preparation (e.g., cutting and sawing). Their sensitivity to air also precludes their persistence on the surface, in naturally weathered outcrops that are exposed to the atmosphere on pedogenic time scales. Therefore, hand specimens collected during field work, even if they previously contained the ferrous hydroxychlorides, may have already lost these minerals. In this work, we detected these minerals only in inclusions enclosed in quartz or in drill cores. This limitation has to be taken into account when the abundance and the role of these minerals is evaluated. Raman spectroscopy can be now used as a simple, fast, and reproducible tool for their quick and non-destructive recognition in geological and archaeological materials.

Acknowledgements

Bernhardt Saini-Eidukat and an anonymous reviewer are thanked for their helpful reviews. Daniel Harlov is acknowledged for editorial handling. This work was supported by the by the grant VEGA-1/0313/20 and by the ERDF grant ITMS 26240220086. Andrew H. Rankin is acknowledged

for his help during early studies of the hibbingite-like mineral in brine inclusions at the School of Earth Sciences and Geography, Kingston University, Kingston upon Thames, United Kingdom in 2001.

References cited

Anselmi, B., Mellini, M., and Viti, C. (2000) Chlorine in the Elba, Monti Livornesi and Murlo serpentines: evidence for sea-water interaction. European Journal of Mineralogy, 12, 137-146.

Bakos, F., Fuchs, P., Hanes, R., Žitňan, P., and Konečný V. (2010) Au-porphyry mineralization in the mantle of the Štiavnica stratovolcano (Western Carpathians). Mineralia Slovaca, 42, 1–14.

Ballhaus, C.G., and Stumpfl, E.F. (1986) Sulfide and platinum mineralization in the Merensky Reef: evidence from hydrous silicates and fluid inclusions. Contributions to Mineralogy and Petrology, 94, 193-204.

Bonifacie, M., Busigny, V., Mével, C., Philippot, P., Agrinier, P., Jendrzejewski, N., Scambelluri, M., and Javoy, M. (2008) Chlorine isotopic composition in seafloor serpentinites and high-pressure metaperidotites. Insights into oceanic serpentinization and subduction processes. Geochimica et Cosmochimica Acta, 72, 126-139.

Brown, G.E., Henrich, V.E., Casey, W.H., Clark, D.L., Eggleston, C., Felmy, A., Goodman, D.W., Grätzel, M., Maciel, G., McCarthy, M.I., Nealson, K.H., Sverjensky, D.A., Toney, M.F., and Zachara, J.M. (1999) Metal Oxide surfaces and their interactions with aqueous solutions and microbial organisms. Chemical Reviews, 99, 77–174.

Buchwald, V.F. (1989) Mineralogi og Reaktionsmodeller ved Komosion of Jordfundne Jerngenstande (Meteoritter og Oldsager). In Yearbook, Danish Metallurgical Society, 41-72.

Buchwald, V.F., and Koch, C.B. (1995) Hibbingite (β-$Fe_2(OH)_3Cl$), a chlorine-rich corrosion product in meteorites and ancient iron objects. Meteoritics, 30 (5), 493-493.

Campos, E., Touret, J.L.R., Nikogosian I., and Delgado, J. (2002) Overheated, Cu-bearing magmas in the Zaldívar porphyry-Cu deposit, Northern Chile. Geodynamic consequences. Tectonophysics, 345, 229–251.

Cawthorn, R.G., Luvimbe, C., and Slabbert, M. (2009) Suspected presence of hibbingite in olivine pyroxenites adjacent to the UG2 chromitite, Bushveld Complex, South Africa. Canadian Mineralogist, 47, 1075–1085.

Dahlberg, E.D., and Saini-Eidukat, B. (1991) A chlorine-bearing phase in drill core of serpentinized troctolitic rocks of the Duluth Complex, Minnesota. Canadian Mineralogist, 29, 239-244.

Debret, B., Koga, K.T., Cattani, F., Nicollet, C., van den Bleeken, G., and Schwartz, S. (2016) Volatile (Li, B, F and Cl) mobility during amphibole breakdown in subduction zones. Lithos, 244, 165-181.

de Wolff, P.M. (1953) The crystal structure of $Co_2(OH)_3Cl$. Acta Crystallographica, 6, 359-360.

Farrow, C.E.G., Watkinson, D., and Jones, P. (1994) Fluid inclusions in sulfides from North and South Range Cu-Ni-PGE deposits, Sudbury Structure, Ontario. Economic Geology, 89, 647-655.

Fleet, M.E. (1975) The crystal structure of paratacamite, $Cu_2(OH)_3Cl$. Acta Crystallographica, B31, 183-187.

Godel, B. (2015) Platinum-group element deposits in layered intrusions: recent advances in the understanding of ore forming processes. In B. Charlier, O. Namur, R. Latypov, C. Tegner, Eds., Layered Intrusions, Springer, Dordrecht, 379-432.

Gustafson, L.B. and Hunt, J.P. (1975) The porphyry copper deposit at El Salvador, Chile. Economic

Geology, 70, 857-912.

Hanes, R., Bakos, F., Fuchs, P., Žitňan, P., and Konečný, V. (2010) Exploration results of Au porphyry mineralizations in the Javorie Stratovolcano. Mineralia Slovaca, 42, 15–33.

Hanley, J.J. and Mungall, J.E. (2003) Chlorine enrichment and hydrous alteration of the Sudbury Breccia hosting footwall Cu-Ni-PGE mineralization at the Fraser mine, Sudbury, Ontario, Canada. Canadian Mineralogist, 41, 857-881

Holland, J.B., and Redfern, S. (1997) Unit cell refinement from powder diffraction data: the use of regression diagnostics. Mineralogical Magazine, 61, 65-77.

Huang, R.F., Sun, W.D., Zhan, W.H., Ding, X., Zhu, J.H., and Liu, J.Q. (2017) Influence of temperature, pressure, and fluid salinity on the distribution of chlorine into serpentine minerals. Journal of Asian Earth Sciences, 145, 101-110.

Jambor, J.L., Dutrizac, J.E., Roberts, A.C., Grice, J.D., and Szymański, J.T. (1996) Clinoatacamite, a new polymorph of $Cu_2(OH)_3Cl$, and its relationship to paratacamite and "anarakite". Canadian Mineralogist, 34, 61-72.

Kawohl, A., and Frimmel, H.W. (2016) Isoferroplatinum-pyrrhotite-troilite intergrowth as evidence of desulfurization in the Merensky Reef at Rustenburg (western Bushveld Complex, South Africa). Mineralogical Magazine, 80, 1041-1053.

Koděra, P., Rankin, A.H., and Lexa, J., (1998) Evolution of fluids responsible for iron skarn mineralisation: An example from the Vyhne-Klokoč deposit (Western Carpathians, Slovakia). Mineralogy and Petrology, 64, 119-147.

Koděra, P., Rankin, A.H., and Murphy, P.J. (2003): Identification of some Fe-bearing daughter minerals in fluid inclusions using Raman spectroscopy. Abstracts of the “XVII ECROFI conference”, Acta Mineralogica-Petrographica, Abstract Series, 2, 101-102.

Koděra, P., Lexa, J., Rankin, A.H., and Fallick, A.E. (2004) Fluid evolution in a subvolcanic granodiorite pluton related to Fe and Pb–Zn mineralization, Banská Štiavnica ore district, Slovakia. Economic Geology, 99, 1745-1770.

Koděra, P., Lexa, J., and Fallick, A.E. (2010) Formation of the Vysoká-Zlatno Cu-Au skarn-porphyry deposit, Slovakia. Mineralium Deposita, 45, 817–843.

Koděra, P., Heinrich, C.A., Wälle, M., and Lexa, J. (2014) Magmatic salt melt and vapour: Extreme fluids forming porphyry gold deposits in shallow volcanic settings. Geology, 42, 495–498.

Koděra, P., Takács, A., Váczi, T., Luptáková, J., and Antal, P. (2015) Mineral composition of salt melt inclusions of the porphyry gold deposit Biely Vrch (Slovakia). In Extended Abstracts Volume of the XXIII ECROFI conference, p. 86–87, Leeds.

Koděra, P., Takács, Á., Racek, M., Šimko, F., Luptáková, J., Váczi, T., and Antal, P. (2017) Javorieite, $KFeCl_3$: a new mineral hosted by salt melt inclusions in porphyry gold systems. European Journal of Mineralogy, 29, 995-1004.

Koděra, P., Kozák, J., Brčeková, J., Chovan, M., Lexa, J., Jánošík, M., Biroň, A., Uhlík, P., and Bakos, F. (2018) Distribution and composition of gold in porphyry gold systems: example from the Biely Vrch deposit, Slovakia. Mineralium Deposita, 53, 1193–1212.

Konečný, V., Bezák, V., Halouzka, R., Konečný, P., Mihaliková, A., Marcin, D., Iglárová, Ľ., Panáček, A., Štohl, J., Žáková, E., Galko, I., Rojkovičová, Ľ., and Onačila, D. (1998) Explanations to the geological map of Javorie 1: 50 000, 304 p Geological Survey of the Slovak Republic, Bratislava.

Kozák, J., Koděra, P., Lexa, J., Bakos, F., Molnár, L., and Wälle, M. (2017) Porphyry gold system of Beluj in the mantle of the Štiavnica stratovolcano (Slovakia). Acta Geologica Slovaca, 9, 45-61.

Krivovichev, S.V., Hawthorne, F.C., and Williams, P.A. (2017) Structural complexity and crystallization: the Ostwald sequence of phases in the $Cu_2(OH)_3Cl$ system (botallackite–atacamite–clinoatacamite). Structural Chemistry, 28, 153-159.

Kubozono, H., Zheng, X.G., Yamada, H., and Xu, C.N. (2006) Structural analysis for novel materials exhibiting exotic properties. II. A structural study of new geometrically frustrated spin systems $M_2Cl(OH)_3$. Reports of the Faculty of Science and Engineering, Saga University, 35, 13.

Kurosawa, M., Sasa, K., Shin, K., and Ishii, S. (2016) Trace-element compositions and Br/Cl ratios of fluid inclusions in the Tsushima granite, Japan: Significance for formation of granite-derived fluids. Geochimica et Cosmochimica Acta, 182, 216–239.

Lee, M.R., and Bland, P.A. (2004) Mechanisms of weathering of meteorites recovered from hot and cold deserts and the formation of phyllosilicates. Geochimica et Cosmochimica Acta, 68, 893–916.

Mikhailenko, D.S., Korsakov, A.V., and Golonin, A.V. (2016) Raman spectroscopic study of mineralogy “non-fresh” salty kimberlites from Udachnaya pipe. P. 15, Abstract Volume of the conference GeoRaman 2016, Novosibirsk.

Mogessie, A.M., and Stumpfl, E.F. (1992) Platinum group element and stable isotope geochemistry of PGM-bearing troctolitic rocks of the Duluth Complex, Minnesota. Australian Journal of Earth Sciences, 39, 315-325.

Neff, D., Dillmann, P., Bellot-Gurlet, L., and Beranger, G. (2005) Corrosion of iron archaeological artefacts in soil: characterisation of the corrosion system. Corrosion Science, 47, 515-535.

Nemer, M.B., Xiong, Y., Ismail, A.E., and Jang, J.H. (2011) Solubility of $Fe_2(OH)_3Cl$ (pure-iron endmember of hibbingite) in NaCl and Na_2SO_4 brines. Chemical Geology, 280, 26-32.

Oswald, H.R., and Feitknecht, W. (1964) Über die Hydroxidhalogenide $Me_2(OH)_3Cl$, -Br, -J zweiwertiget Metalle (Me = Mg, Ni, Co, Cu, Fe, Mn). Helvetica Chimica Acta, 47, 272–289.

Oswald, H.R., and Guenter, J.R. (1971) Crystal data on paratacamite γ-$Cu_2(OH)_3Cl$. Journal of Applied Crystallography, 4, 530-531.

Pollard, A.M., Thomas, R.G., and Williams, P.A. (1989) Synthesis and stabilities of the basic copper(II) chlorides atacamite, paratacamite and botallackite. Mineralogical Magazine, 53, 557-563

Refait, P., and Génin, J.M.R. (1997) The mechanisms of oxidation of ferrous hydroxychloride β-$Fe_2(OH)_3Cl$ in chloride-containing aqueous solution: the formation of β-FeOOH akaganeite; an X-ray diffraction, Mössbauer spectroscopy and electrochemical study, Corrosion Science, 39, 539–553.

Réguer, S., Dillmann, P., Mirambet, F., and Bellot-Gurlet, L. (2005) Local and structural characterisation of chlorinated phases formed on ferrous archaeological artefacts by μXRD and μXANES. Nuclear Instruments and Methods in Physics Research B, 240, 500–504.

Réguer, S., Neff, D., Bellot-Gurlet, L., and Dillmann, P. (2007) Deterioration of iron archaeological artefacts: micro-Raman investigation on Cl-containing corrosion products. Journal of Raman Spectroscopy, 38, 389–397.

Réguer, S, Mirambet, F., Rémazeilles, C., Vantelon, D., Kergourlaya, F., Neff, D., and Dillmann, P. (2015) Iron corrosion in archaeological context: Structural refinement of the ferrous hydroxychloride β-$Fe_2(OH)_3Cl$. Corrosion Science, 100, 589-598.

Rémazeilles, C., and Refait, P. (2008) Formation, fast oxidation and thermodynamic data of Fe(II) hydrochlorides. Corrosion Science, 50, 856-864.

Rémazeilles, C., Neff, D., Kergourlay, F., Foy, E., Conforto, E., Guilminot, E., Reguer, S., Refait, P., and Dillman, P. (2009) Mechanisms of long-term anaerobic corrosion of iron archaeological artefacts in seawater. Corrosion Science, 51, 2932–2941.

Ripley, E.M. (1990) Platinum-group element geochemistry of Cu-Ni mineralization in the Basal Zone of the Babbitt Deposit, Duluth Complex, Minnesota. Economic Geology, 85, 830-841.

Rucklidge, J.C., and Patterson, G.C. (1977) The role of chlorine in serpentinization. Contributions to Mineralogy and Petrology, 65, 39–44.

Saini-Eidukat, B., Kucha, H., and Keppler, H. (1994) Hibbingite, γ-$Fe_2(OH)_3Cl$, a new mineral from the Duluth Complex, Minnesota, with implications for oxidation of iron bearing compounds and transport of metals. American Mineralogist, 79, 555–561.

Saini-Eidukat, B., Rudashevsky, N.S., and Polozov, A.G. (1998) Evidence for hibbingite–kempite solid solution. Mineralogical Magazine, 62, 251–255.

Schlüter, J., Klaska, K.-H., and Gebhard, G. (2000) Belloite, Cu(OH)Cl, a new mineral from Sierra Gorda, Antofagasta, Chile. Neues Jahrbuch für Mineralogie, Monatshefte, 2, 67-73.

Sharp, Z.D., and Barnes, J.D. (2004) Water-soluble chlorides in massive seafloor serpentinites: a source of chloride in subduction zones. Earth and Planetary Science Letters, 226, 243-254.

Springer, G. (1989) Chlorine-bearing and other uncommon minerals in the Strathcona deep copper zone, Sudbury district, Ontario. Canadian Mineralogist, 27, 311–313.

Vanhanen, E. (2001): Geology, mineralogy and geochemistry of the Fe-Co-Au-(U) deposits in the Paleoproterozoic Kuusamo Schist Belt, northeastern Finland. Geological Survey of Finland, Bulletin, 399 p.

Zhitova, L., Kinnaird, J.A., Gora, M., and Shevko, E.P. (2016) Magmatogene fluids of metal-bearing reefs in the Bushveld Complex, South Africa: Based on research data on fluid inclusions in quartz. Geology of Ore Deposits, 58, 58–81.

Zubkova, N.V., Pekov, I.V., Sereda, E.V., Yapaskurt, V.O., and Pushcharovsky, D,Yu. (2019) The crystal structure of hibbingite, orthorhombic $Fe_2Cl(OH)_3$. Zeitschrift für Kristallographie - Crystalline Materials, 234, 379–382.

Tables

Table 1: The Raman shift of bands (in cm^{-1}) of ferrous hydroxychloride, determined in fluid (a – d, i) and salt melt inclusions (e – h) worldwide. Based on the results in this study, the Raman spectra belong to the mineral hibbingite.

a	**b**	**c**	**d**	**e**	**f**	**g**	**h**	**i**
-	-	-	-	-	*81*	-	*84*	*82*
-	-	-	-	-	-	-	*89*	-
-	-	-	-	-	-	-	*109*	*110*
-	-	-	*141*	-	-	-	*137*	141
-	-	-	*147*	-	-	-	-	-
-	-	-	-	-	-	-	*165*	*164*
-	-	-	*188*	-	-	-	*186*	-
-	**199**	**199**	**200**	**199**	**199**	**199**	**198**	**199**
-	-	-	-	-	-	-	*279*	*277*
-	385	385	387	385	385	386	385	*386*
-	-	-	*439*	-	-	-	*438*	*438*
-	-	-	-	-	-	-	*728*	-
-	-	-	*783*	-	-	-	*776*	*775*
3448	**3449**	**3450**	**3452**	**3450**	**3452**	**3451**	**3451**	**3449**

Note: The bold numbers are the strongest Raman bands. The normal numbers are medium bands. Numbers in italics are weak bands. a. Chorloque Sn-porphyry deposit (Bolivia; Koděra et al., 2003); b. Sn-W-Fe-bearing vein related to the Dartmoor granite (UK; Koděra et al. 2003); c. Endoskarn, Vyhne-Klokoč Fe-skarn deposit (Slovakia; Koděra et al. 2003); d. Vysoká-Zlatno Cu-Au skarn-porphyry deposit (Slovakia; Koděra et al. 2010); e. Beluj Au-porphyry occurrence; Kozák et al. 2017; f. Slatinské Lazy Au-porphyry occurrence (this study); g. Králová Au-porphyry occurrence (this

study); h. Biely Vrch Au-porphyry deposit (Koděra et al. 2015 and this study; i - Tsushima granite (Japan; Kurosawa et al. 2016)

Table 2: Representative EMP analyses of parahibbingite from the Karee mine in the Bushveld Complex.

anal. #	**1**	**2**	**3**	**4**	**5**	**6**	**7**	**8**	**9**	**10**	**11**	**12**
Fe	54.12	54.29	53.49	51.98	51.96	52.00	52.53	52.63	53.01	52.54	52.66	52.93
Mn	0.32	0.33	0.22	0.33	0.35	0.49	0.62	0.33	0.32	0.35	0.62	0.38
Mg	0.09	0.05	0.04	0.02	0.13	0.20	0.06	0.08	0.05	0.08	0.03	0.02
Si	0.03	0.03	0.04	0.00	0.24	0.35	0.13	0.03	0.03	0.19	0.10	0.06
Al	0.01	0.00	0.00	0.00	0.00	0.00	0.00	0.00	0.00	0.00	0.00	0.00
Cl	15.37	16.13	17.20	18.34	18.39	17.98	17.22	16.31	16.98	17.18	17.36	17.22
F			0.02	0.19	0.18	0.15						
Na	0.05	0.02	0.02	0.06	0.03	0.07	0.00	0.04	0.02	0.00	0.00	0.01
K	0.01	0.01	0.01	0.00	0.00	0.00	0.00	0.01	0.00	0.00	0.00	0.01
Ca	0.68	0.25	0.28	0.13	0.02	0.04	0.06	0.44	0.25	0.12	0.06	0.15
Ti	0.00	0.00	0.01	0.00	0.00	0.02	0.00	0.01	0.01	0.02	0.00	0.02
Cr	0.01	0.00	0.00	0.02	0.03	0.01	0.03	0.01	0.00	0.01	0.03	0.00
Ni				0.00	0.00	0.00						
OH*	26.49	25.81	24.74	23.11	23.15	23.58	24.25	24.92	24.62	24.19	24.23	24.37
Total	97.19	96.93	96.07	94.17	94.48	94.89	94.90	94.81	95.28	94.68	95.10	95.17
Normalized on the basis of 2 divalent cations (Fe+Mn+Mg+Ca) per formula unit												
Fe	1.944	1.970	1.973	1.977	1.967	1.951	1.965	1.956	1.969	1.968	1.968	1.974
Mn	0.012	0.012	0.008	0.013	0.014	0.019	0.024	0.012	0.012	0.013	0.024	0.015
Mg	0.007	0.004	0.003	0.002	0.011	0.017	0.005	0.007	0.004	0.007	0.003	0.002
Si	0.002	0.002	0.003	0	0.018	0.026	0.01	0.002	0.002	0.014	0.007	0.004
Al	0.001	0	0	0	0	0	0	0	0	0	0	0
Cl	0.87	0.922	0.999	1.099	1.097	1.063	1.015	0.955	0.994	1.014	1.022	1.012
F				0.011	0.011	0.009						
Na	0.004	0.002	0.002	0.005	0.003	0.006	0	0.004	0.002	0	0	0.001
K	0	0	0.001	0	0	0	0	0	0	0	0	0.001
Ca	0.034	0.012	0.014	0.007	0.001	0.002	0.003	0.023	0.013	0.006	0.003	0.008
Ti	0	0	0	0	0	0.001	0	0	0	0.001	0	0.001
Cr	0	0	0	0.001	0.001	0.001	0.001	0	0	0	0.001	0
Ni				0	0	0						
OH	3.125	3.075	2.996	2.886	2.878	2.906	2.978	3.041	3.003	2.976	2.972	2.984

Note: The analyses 5 and 6 contain a minor admixture (inclusions) of the host mineral talc. The totals lower than 100 % are explained by fine-grained nature and porosity of the parahibbingite aggregates.

* calculated from stoichiometry

Table 3: The Raman shift of main bands (in cm^{-1}) of parahibbingite from the Karee mine in the Bushveld Complex compared to main bands of the β-form of $Fe_2(OH)_3Cl$ created as corrosion on archaeological artefacts[a] and to main bands of synthetic β-$Fe_2(OH)_3Cl$[b].

parahibbingite	**β-$Fe_2(OH)_3Cl$ (corrosion)**	**β-$Fe_2(OH)_3Cl$ (synthetic)**	**Suggested assignment**
124[c]	127	**127**	?
160[c]	**160**	**163**	O-Fe-O bending mode
-	200	-	?
317	318	320	Fe-Cl stretching vibration
424	423	425	Fe-Cl stretching vibration
613	618	622	Fe-O stretching vibration
816	804	-	Hydroxyl deformation mode
3550	**3552**	**3550**	Hydroxyl stretching vibration
3561	**3564**	**3560**	Hydroxyl stretching vibration

Note: Assignment of bands is based on Réguer et al. (2007). [a] Réguer et al. 2007, [b] Rémazeilles and Refait 2008, [c] The intensity of these bands varies due to crystal orientation.

Table 4. TEM-EDX point analyses of hibbingite daughter mineral (wt% normalized, neglecting hydrogen) from a salt melt inclusion hosted by a quartz vein from the Biely Vrch porphyry gold deposit (sample DVE-51/475.0).

anal. #	**1**	**2**	**3**
Fe	57.8	54.5	60.6
Cl	17.7	23.2	15.1
O	24.5	22.3	24.3
Total	100.0	100.0	100.0
Normalized on the basis of 6 atoms plus hydrogen by charge balance			
Fe	2.02	1.93	2.15
Cl	0.98	1.30	0.84
O	3.00	2.77	3.01
H	*2.93*	*2.97*	*2.56*

Note: Sodium and a stoichiometric amount of Cl, most probably originating from the surrounding halite, were removed from the analyses 2 and 3 and they were renormalized thereafter.

Table 5: Electron diffraction data of a hibbingite daughter mineral in salt melt inclusion from the Biely Vrch porphyry gold deposit compared to calculated diffraction data from hibbingite.

d measured [Å]	d calc [Å][a]	d calc [Å][b]	{hkl}
6.31	6.31	6.337	1 0 0 E
5.63	5.62	5.597	0 1 1
n. obs.	5.20	5.245	1 0 1
4.89	4.72	4.695	1 1 0 E
n. obs.	4.60	4.673	0 0 2
4.32	4.20	4.195	1 1 1
3.92	3.72	3.761	1 0 2
2.72	2.75	2.757	2 1 1

[a] Saini-Eidukat et al. (1994), [b] Zubkova et al. (2019) ; E extinct reflection – observable due to double diffraction; n. obs. = not observable due to grain orientation and tilt limitations.

Table 6: Unit-cell parameters (Å) of parahibbingite and hibbingite obtained in this work compared to the published parameters of β-$Fe_2(OH)_3Cl$ and hibbingite (γ-$Fe_2(OH)_3Cl$).

Reference/Cell parameter	*a*	*b*	*c*
Parahibbingite			
this study (Karee mine sample)	6.94		14.5
Oswald and Feitknecht (1964)	6.93		14.71
Réguer et al. (2015) – corrosion sample	6.942		14.698
Réguer et al. (2015) – synthetic sample	6.928		14.761
Hibbingite			
this study (Biely Vrch sample)	6.30	7.12	9.89
Saini-Eidukat et al. (1994)	6.31	7.1	9.20
Zubkova et al. (2019)	6.3373	6.9892	9.3457

Table 7: Comparison of the basic properties of parahibbingite and hibbingite.

Data type	Parahibbingite	Hibbingite
Chemical formula	β-$Fe_2(OH)_3Cl$	γ-$Fe_2(OH)_3Cl$
Crystal system	Trigonal [1]	Orthorhombic [2]
Space group	*R-3m* [1]	*Pnma* [3]

Unit-cell parameters (Å)	a = 6.94, c = 14.5 [4]	a = 6.3373, b = 6.9892, c = 9.3457 [1]
Main diffraction lines (d spacing) [Å]	2.31(1), 2.82(0.6), 5.55(0.4), 1.74(0.4), 2.94(0.2), 1.85(0.2), 1.53(0.2) [4]	2.37(1), 2.93(0.6), 2.14(0.5), 1.65(0.5), 5.68(0.4) [2]
Main Raman bands (cm^{-1})	124, 160, 3550, 3561 [4]	200, 385, 3452 [5]
Optical data	Greenish [6]	Colorless to pale green [2]

References: [1] – Oswald and Feitknecht (1964), [2] - Saini-Eidukat et al. (1994), [3] Zubkova et al. (2019), [4] - This study, [5] - Koděra et al. (2010), [6] - Buchwald and Koch (1995)

Figure captions

Fig. 1: Comparison of representative Raman spectra of a daughter mineral, recognized in this study as hibbingite, hosted by multisolid fluid inclusions (a - d) and salt melt inclusions (e - i) in quartz from different localities in the world. Also shown are images of corresponding fluid and salt melt inclusions with identified phases. The spectra contain wavenumbers of peaks affiliated to hibbingite, neighboring phases (javorieite – J, rinneite – R) and peaks that belong to the host quartz (Q). The spectra and images were obtained and partially published by Koděra et al. (2003, 2010, 2017), Kozák et al. (2017) and in this study. **a.** Endoskarn, Vyhne-Klokoč Fe-skarn deposit (Slovakia). **b.** Vysoká-Zlatno Cu-Au skarn-porphyry deposit (Slovakia). **c.** Sn-W-Fe-bearing vein related to the Dartmoor granite (UK). **d.** Chorloque Sn-porphyry deposit (Bolivia). **e.** Beluj Au-porphyry occurrence (Slovakia). **f.** Slatinské Lazy Au-porphyry occurrence (Slovakia). **g.** Králová Au-porphyry occurrence (Slovakia). **h-i.** Biely Vrch Au-porphyry deposit (Slovakia). Hib = hibbingite, Hl = halite, Syl = sylvite, Bt = biotite, Fe-hydr = Fe-bearing hydrate, Jav = javoriete, Rin = rinneite, Clc = chlorocalcite, Rok = rokühnite.

Fig. 2: Images of parahibbingite in the sample of pyroxenite from the Bushveld Complex, significantly affected by hydrothermal alteration (sample K-37-19). White labels of minerals are based on EDS and EMP analyses. Yellow labels are based on Raman microanalyses. **a-c.** BSE images (a, c) and reflected light image (b) of the spot studied in detail by combined Raman, EDS/EMP and FIB-TEM analyses. Black

rectangles show the position of the reflected light image (b) and the detailed BSE image of the spot where a parahibbingite foil was cut out by FIB for TEM analyses (c – rotated 120°). **d-i.** BSE images showing the occurrence of parahibbingite and accompanying minerals. Black rectangle in (d) shows the position of the detail in (e). Opx = orthopyroxene, Cum = cummingtonite, Am = Ca-amphiboles, Bt = biotite, Qtz = quartz, Phb = parahibbingite (±hibbingite), Tlc = talc, Cb = carbonate, Spl = spinel, Rt = rutile, Cal = calcite, Dol = dolomite, Sd = siderite, Po = pyrrhotite, Cc = chalcopyrite.

Fig. 3: Typical Raman spectrum of parahibbingite in the sample from the Karee mine (**a, b**) compared to the Raman spectrum of β-$Fe_2(OH)_3Cl$ formed as corrosion on archaeological artefacts (Réguer et al. 2007) (**c**). The Raman spectrum of parahibbingite is also presented as a compilation of two spectra. The second was recorded after a 90° turn from the previous position to evaluate the effect of crystallographic orientation (**d**). Note that the spectra of parahibbingite also include two minor peaks that correspond to Raman scattering of the host talc.

Fig. 4: Typical Raman spectrum of parahibbingite accompanied by hibbingite and talc from the Karee mine (**a, b**) compared to two types of Raman spectra of talc from the same sample (**c, d**) that probably have a different Fe content in talc.

Fig. 5: a. Low-magnification STEM image of the complete TEM foil from a sample from the Karee mine showing a diffraction contrast of the phases present. Single crystals of parahibbingite (dark grey) with a size of less than 1 μm are surrounded by a talc matrix (bright) and orthopyroxene (right rim). **b.** Bright field image of parahibbingite grains showing a lamellar microstructure. The source of this contrast is uncertain.

Fig. 6: Diffraction patterns taken during the TEM session of selected areas (SAED) from the parahibbingite TEM foil taken from the Karee mine (left, see Fig. 3a-c) and the corresponding simulations of electron diffraction patterns of the beta (middle) and gamma (right) phase. **a.** Pattern DP15 - zone axis [1 -1 0] of the β-phase. The zone axis [1 -2 0] γ has a similar geometry, but some of the reflections (e.g., *d* = 4.88 Å, (003) β) are compatible only with the β-phase and some reflections (e.g., 2 1 1) of the γ-phase are missing. **b.** Pattern DP26 - zone axis [1 2 -1] β. The pattern corresponds also to the zone axis [1 -1 1] γ but with an extinction violation. **c.** Pattern DP30 – zone axis [4 -1 2] β. This diffraction pattern is similar but not compatible with the calculated pattern for [2 -1 0] γ. **d.** Pattern DP21 - zone axis [0 0 1] for γ. A subset of reflections is compatible with [4 -4 1] β. This diffraction pattern shows that both polymorphs are present in the sample. This observation is not the result of beam damage, because this diffraction pattern was recorded relatively early in the TEM session.

Fig. 7: Images documenting a salt melt inclusion hosted by a quartz vein from the Biely Vrch porphyry gold deposit (sample DVE-51/475.0) with a hibbingite daughter mineral. Identification of solid phases is based on combined Raman and FIB-SEM-TEM analytical techniques (TEM-EDX, TEM-SAED). **a.** Photomicrograph of the salt melt inclusion in transparent light. **b.** SEM image of the salt melt inclusions after opening by FIB. **c.** Series of images representing EDX maps for selected elements from the area of the inclusion in the red rectangle shown in b. First image in the series is an SEM image. Note that the prismatic hibbingite crystal is predominantly composed of Fe, O, and Cl. The variable intensity of O and Si in quartz (lower part of images) is due to thickness differences in the TEM foil. Hib = hibbingite, Hl = halite, Jav = javoriete, Rin = rinneite, Qtz = quartz.

Fig. 8: Typical EDX spectrum from a point in the hibbingite crystal from the salt melt inclusion from the Biely Vrch deposit shown in Fig. 7. Note that the Cu signal does not belong to the analyzed point, and it comes from grid due to stray radiation.

Fig. 9: Electron diffraction patterns taken from selected areas (SAED) in the hibbingite TEM foil from the salt melt inclusion in the quartz vein sample from the Biely Vrch porphyry gold deposit. Also shown are the corresponding simulations of the electron diffraction patterns (right images). **a.** Electron diffraction pattern from the zone axis [0 -1 -1]. **b.** Electron diffraction pattern from the zone axis [2 -1 -1]. Both diffraction patterns are compatible with published hibbingite electron diffraction data of Saini-Eidukat et al. (1994) and Zubkova et al. (2019).

Figure 1

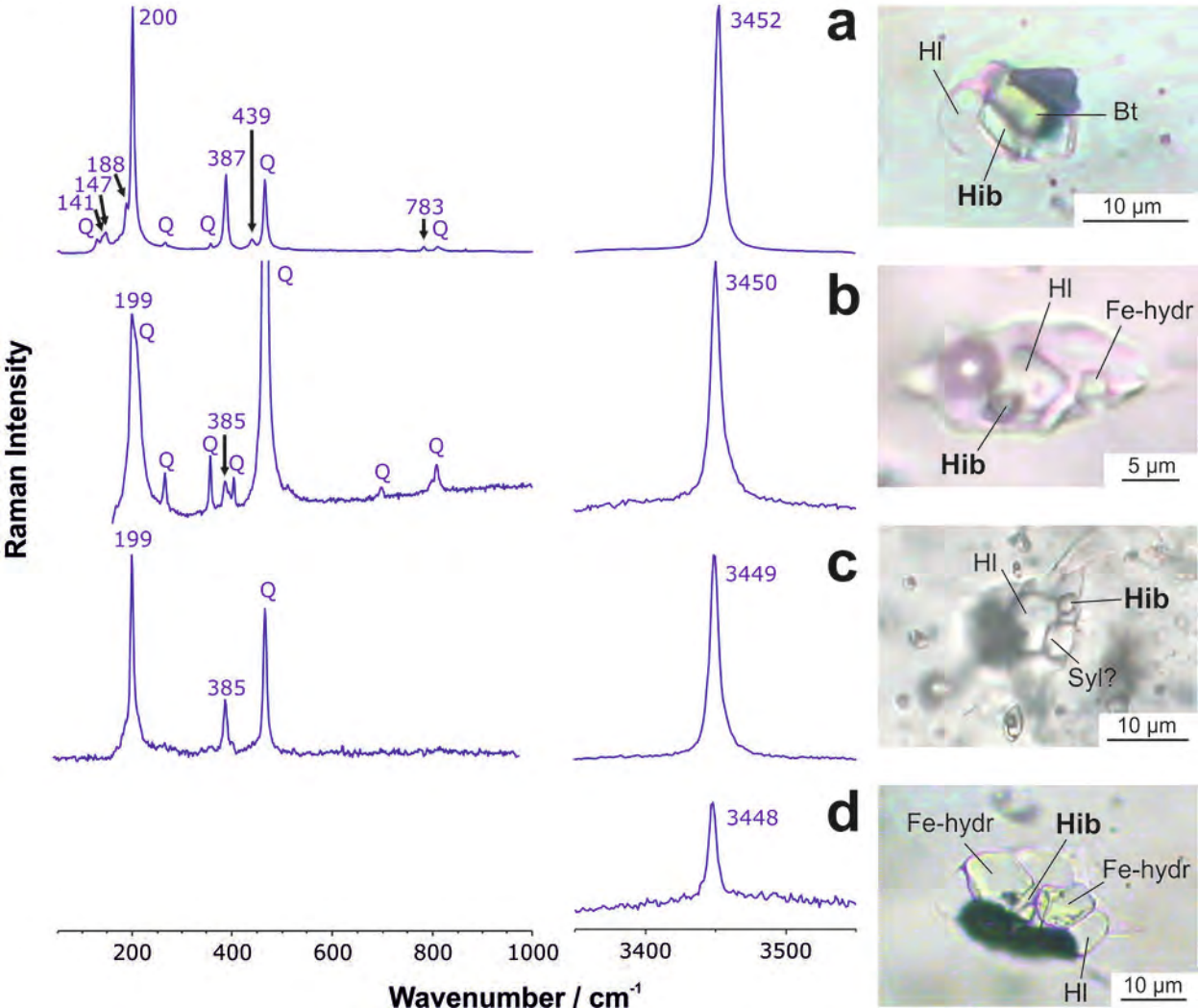
a
200
439
387
188
147
141
Q
783
3452
Hl
Bt
Hib
10 µm
b
199
385
3450
Fe-hydr
5 µm
c
3449
Syl?
d
3448
Raman Intensity
200
400
600
800
1000
3400
3500
Wavenumber / cm-1

Figure 1 cont.

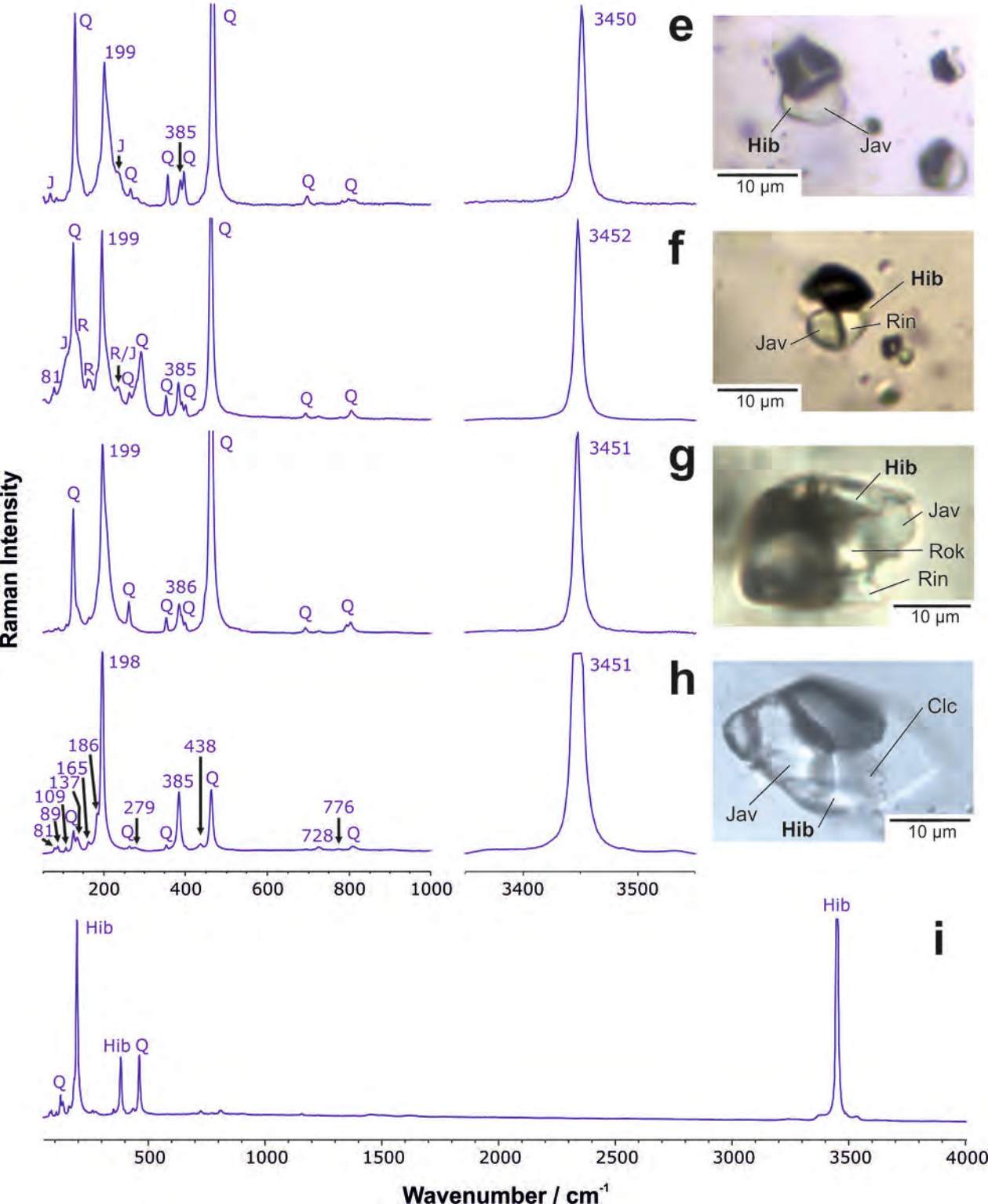

Figure 2

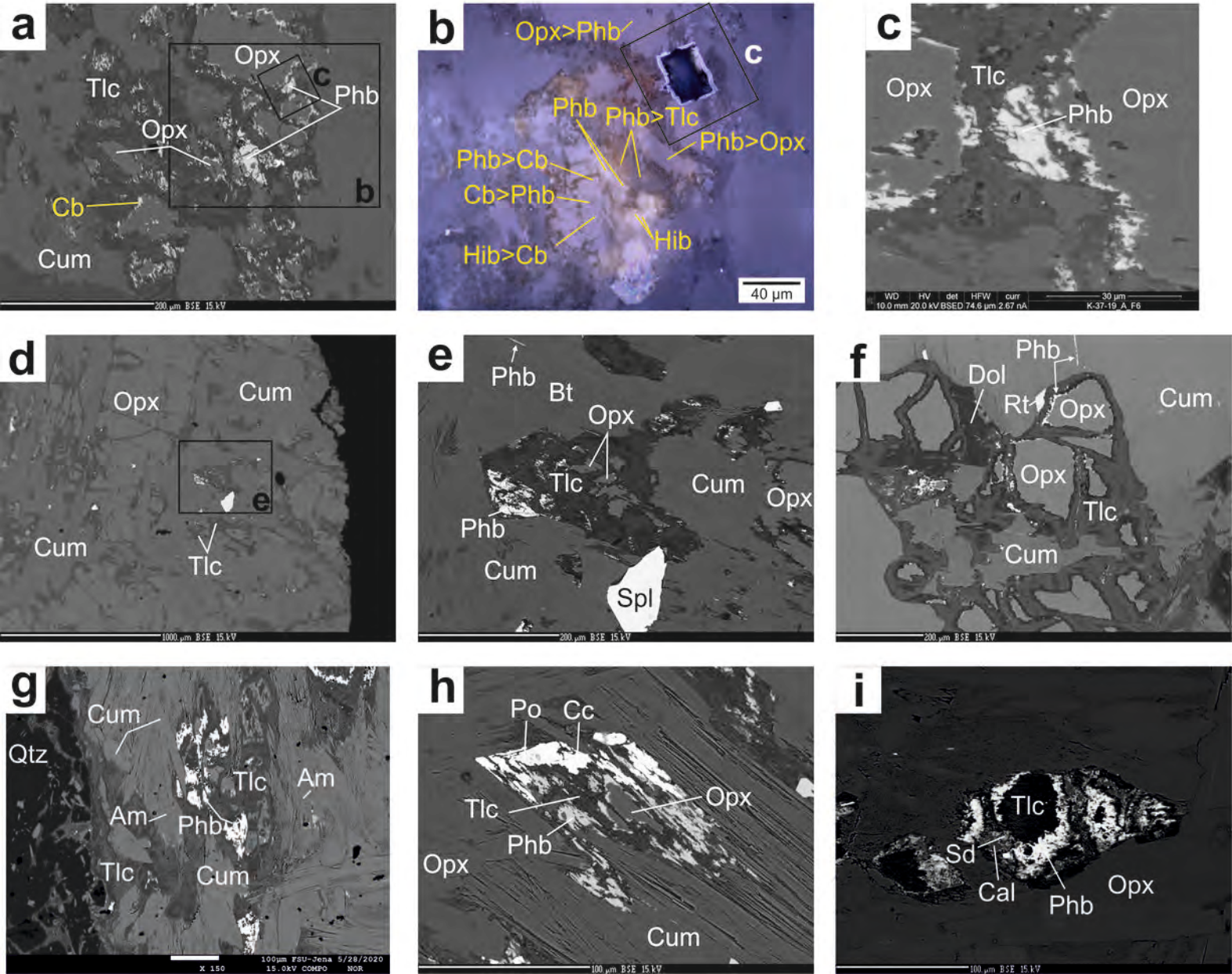
a
Opx
c
Phb
Tlc
Opx
b
Cb
Cum
200 µm BSE 15 kV
b
Opx>Phb
c
Phb
Phb>Tlc
Phb>Opx
Phb>Cb
Cb>Phb
Hib
Hib>Cb
40 µm
c
Opx
Tlc
Opx
Phb
WD HV det HFW curr
10.0 mm 20.0 kV BSED 74.6 µm 2.67 nA
30 µm
K-37-19_A_F6
d
Opx
Cum
e
Cum
Tlc
1000 µm BSE 15 kV
e
Phb
Bt
Opx
Tlc
Cum
Opx
Phb
Cum
Spl
200 µm BSE 15 kV
f
Phb
Dol
Rt
Opx
Cum
Opx
Tlc
Cum
200 µm BSE 15 kV
g
Cum
Qtz
Tlc
Am
Am
Phb
Tlc
Cum
100µm FSU-Jena 5/28/2020
X 150
15.0kV COMPO NOR
h
Po
Cc
Tlc
Opx
Phb
Opx
Cum
100 µm BSE 15 kV
i
Tlc
Sd
Cal
Phb
Opx
100 µm BSE 15 kV

Figure 3

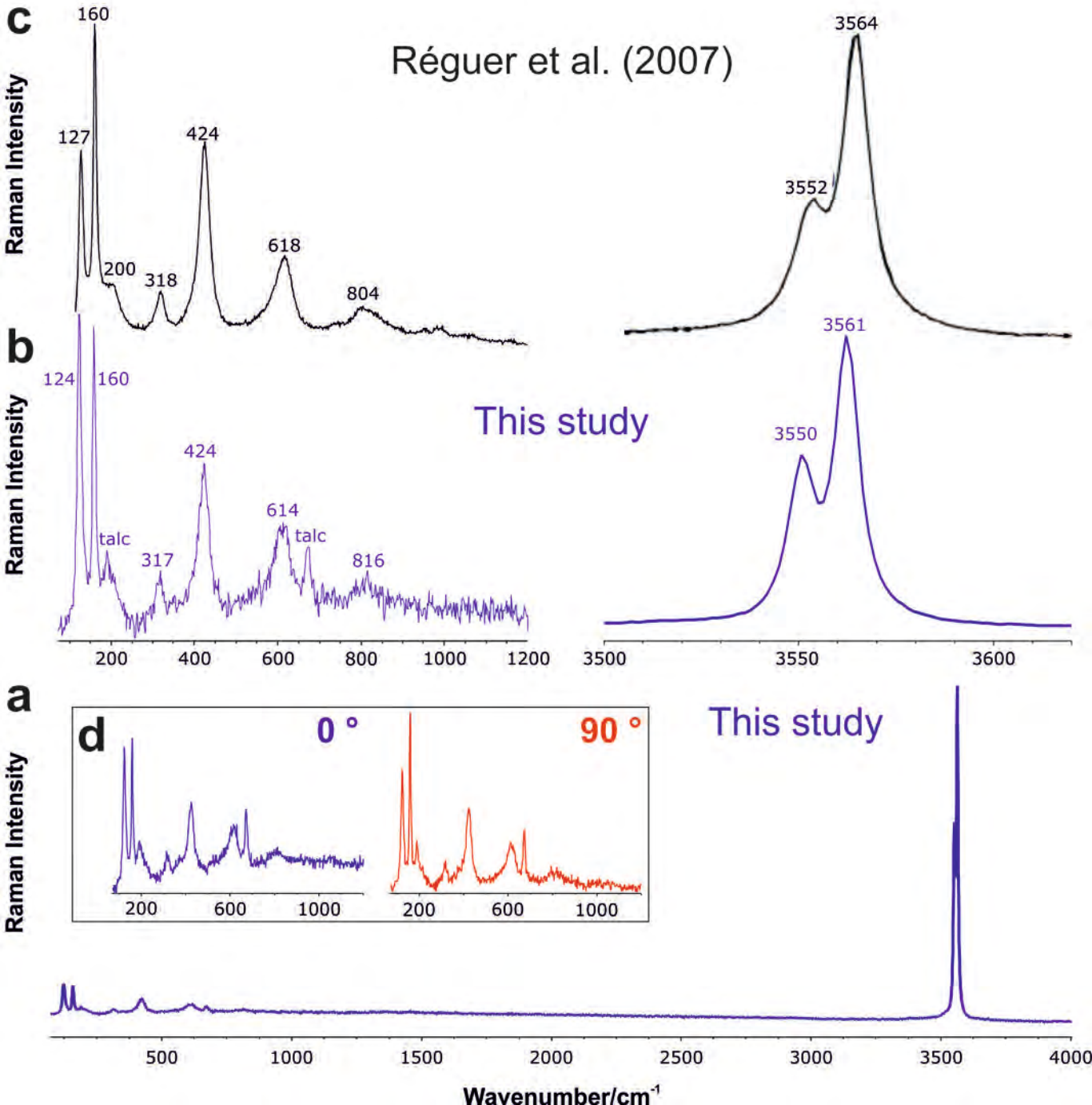
c
Raman Intensity
160
127
200
318
424
618
804
Réguer et al. (2007)
3564
3552
b
Raman Intensity
124
160
talc
317
424
614
talc
816
This study
3561
3550
200
400
600
800
1000
1200
3500
3550
3600
a
Raman Intensity
d
0 °
90 °
200
600
1000
This study
500
1000
1500
2000
2500
3000
3500
4000
Wavenumber/cm-1

Figure 4

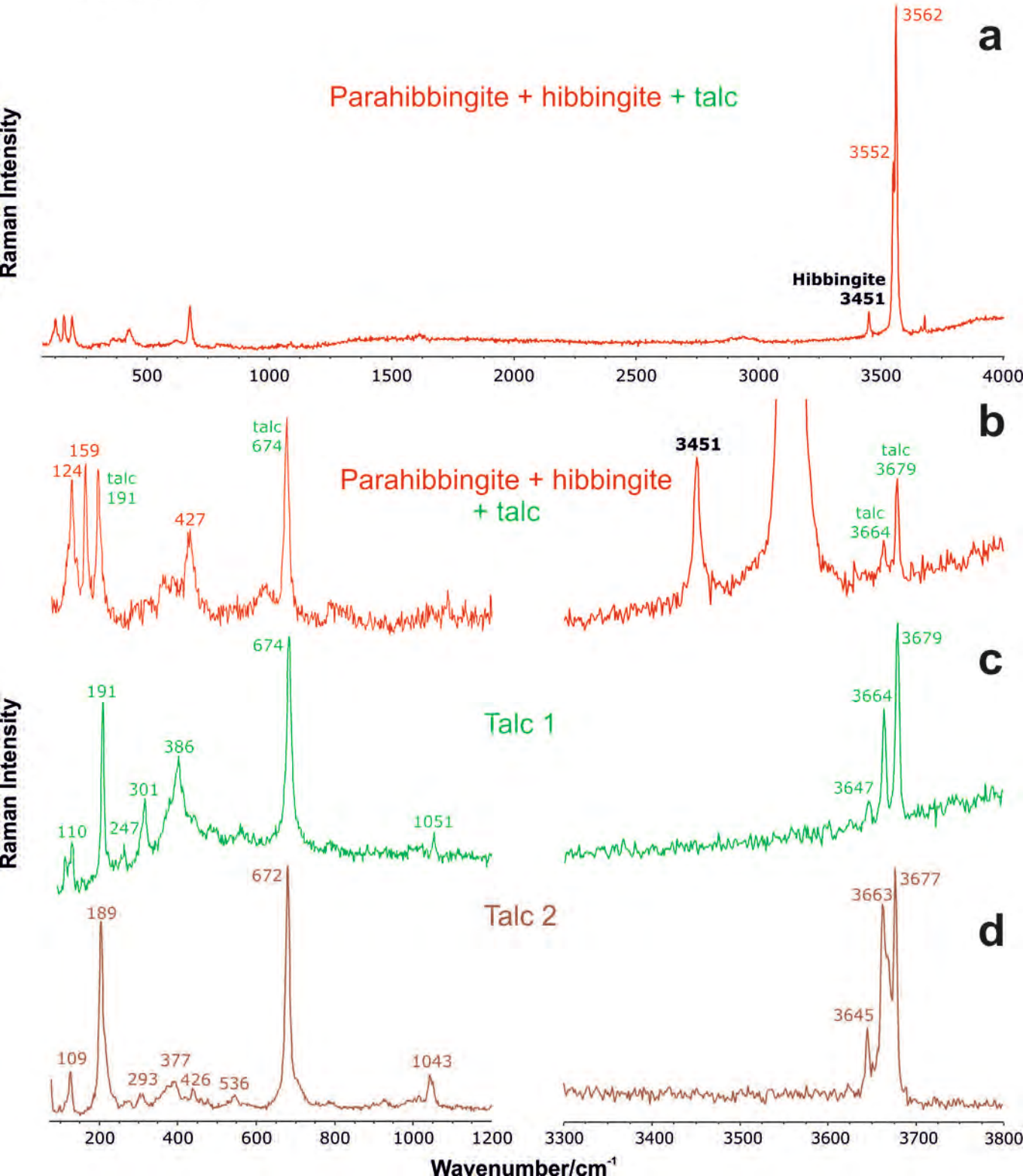
a
Parahibbingite + hibbingite + talc
3562
3552
Hibbingite
3451
Raman Intensity
500
1000
1500
2000
2500
3000
3500
4000
b
Parahibbingite + hibbingite
+ talc
159
124
talc
191
427
talc
674
3451
talc
3679
talc
3664
c
Talc 1
674
191
386
301
110
247
1051
3679
3664
3647
d
Talc 2
672
189
109
377
293
426
536
1043
3663
3677
3645
Raman Intensity
200
400
600
800
1000
1200
3300
3400
3500
3600
3700
3800
Wavenumber/cm-1

Figure 5

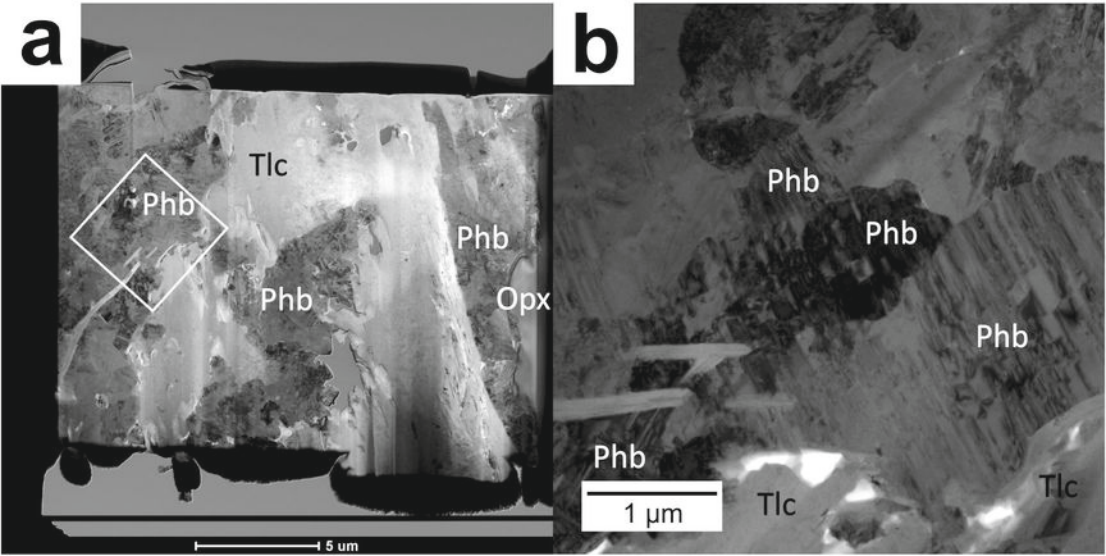

Figure 6

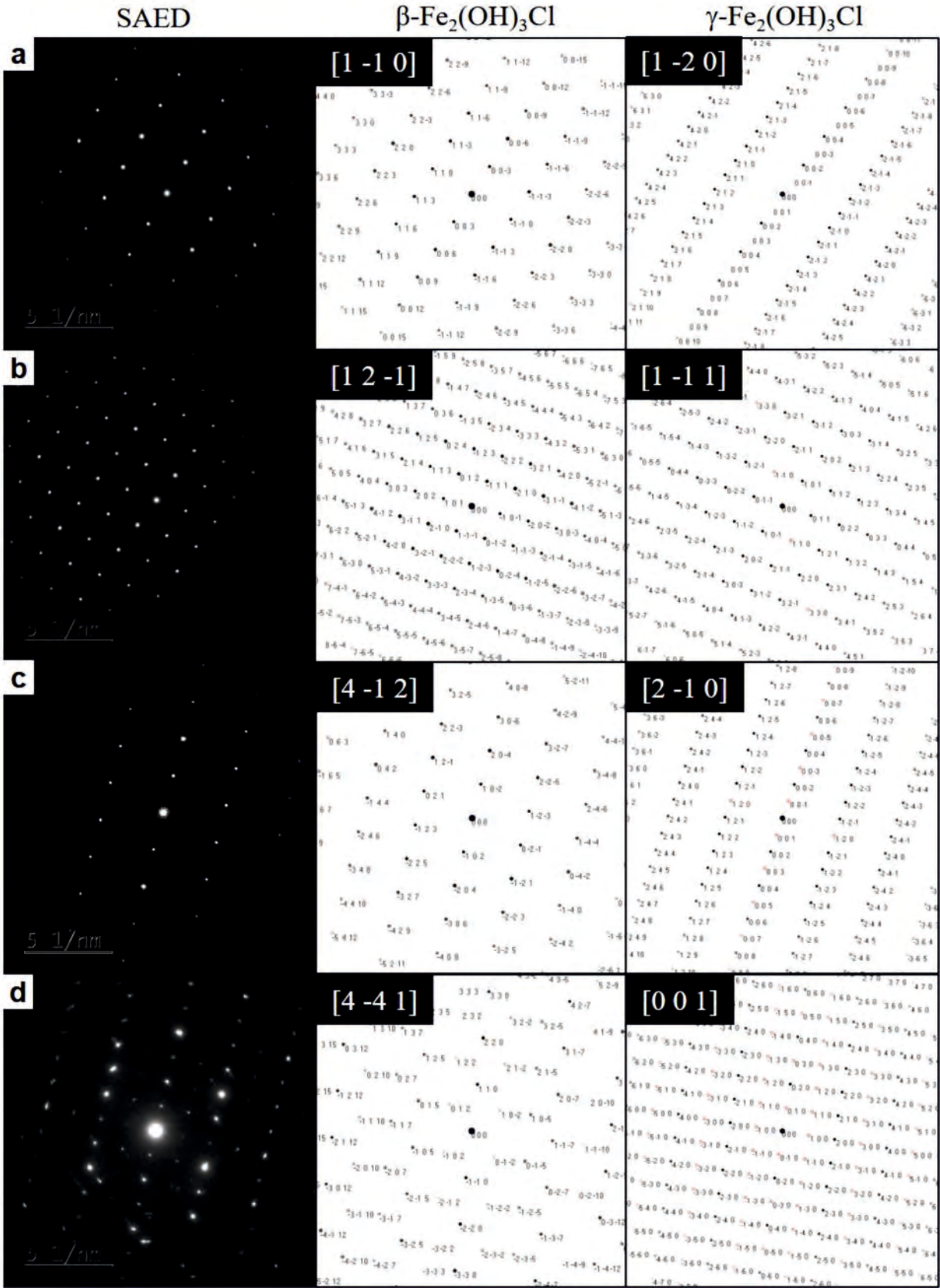
SAED
β-Fe2(OH)3Cl
γ-Fe2(OH)3Cl
a
[1 -1 0]
[1 -2 0]
b
[1 2 -1]
[1 -1 1]
c
[4 -1 2]
[2 -1 0]
d
[4 -4 1]
[0 0 1]
5 1/nm

Figure 7

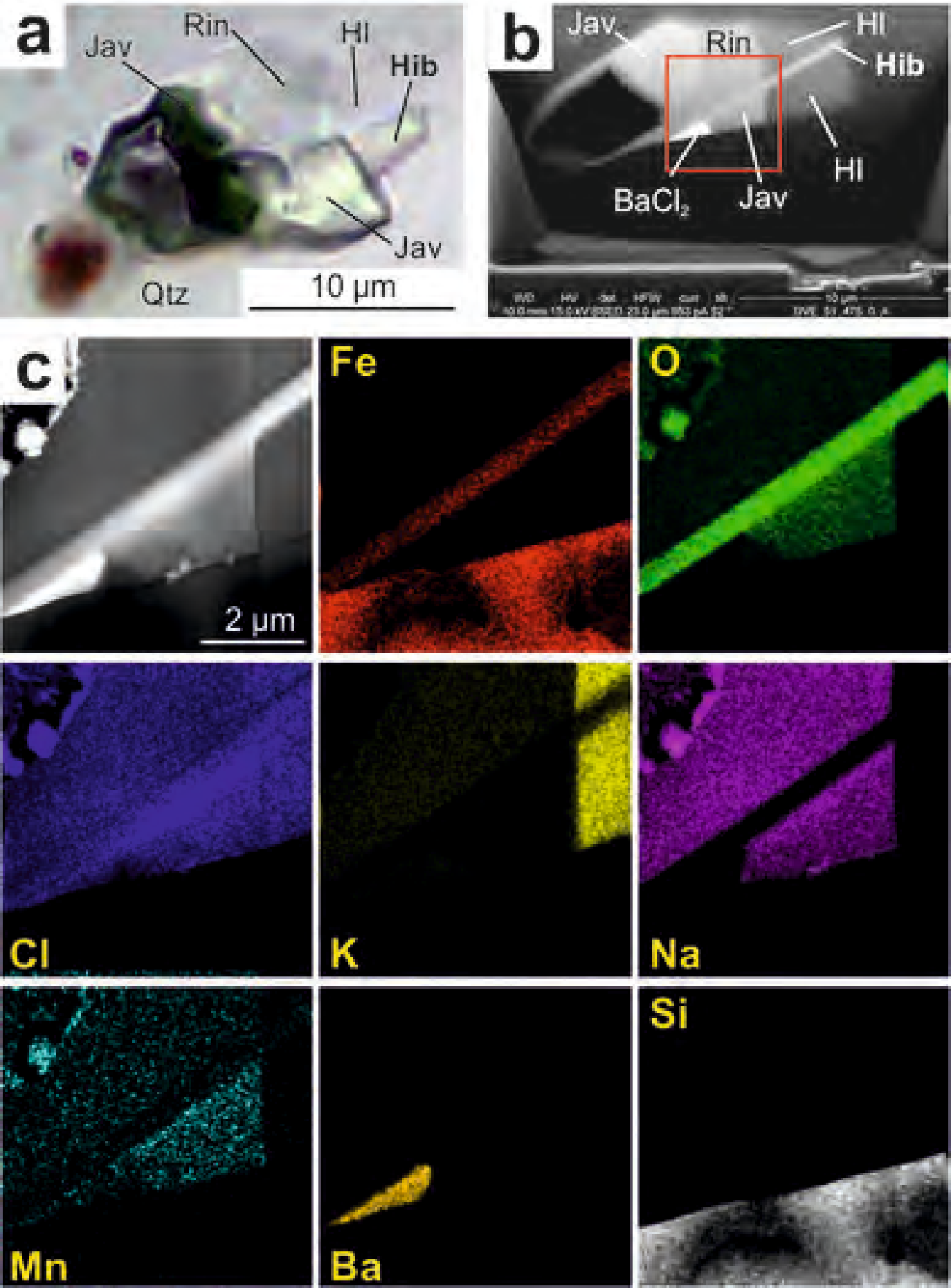
a
Jav
Rin
Hl
Hib
Jav
Qtz
10 µm
b
Jav
Rin
Hl
Hib
Hl
BaCl2
Jav
c
2 µm
Fe
O
Cl
K
Na
Mn
Ba
Si

Figure 8

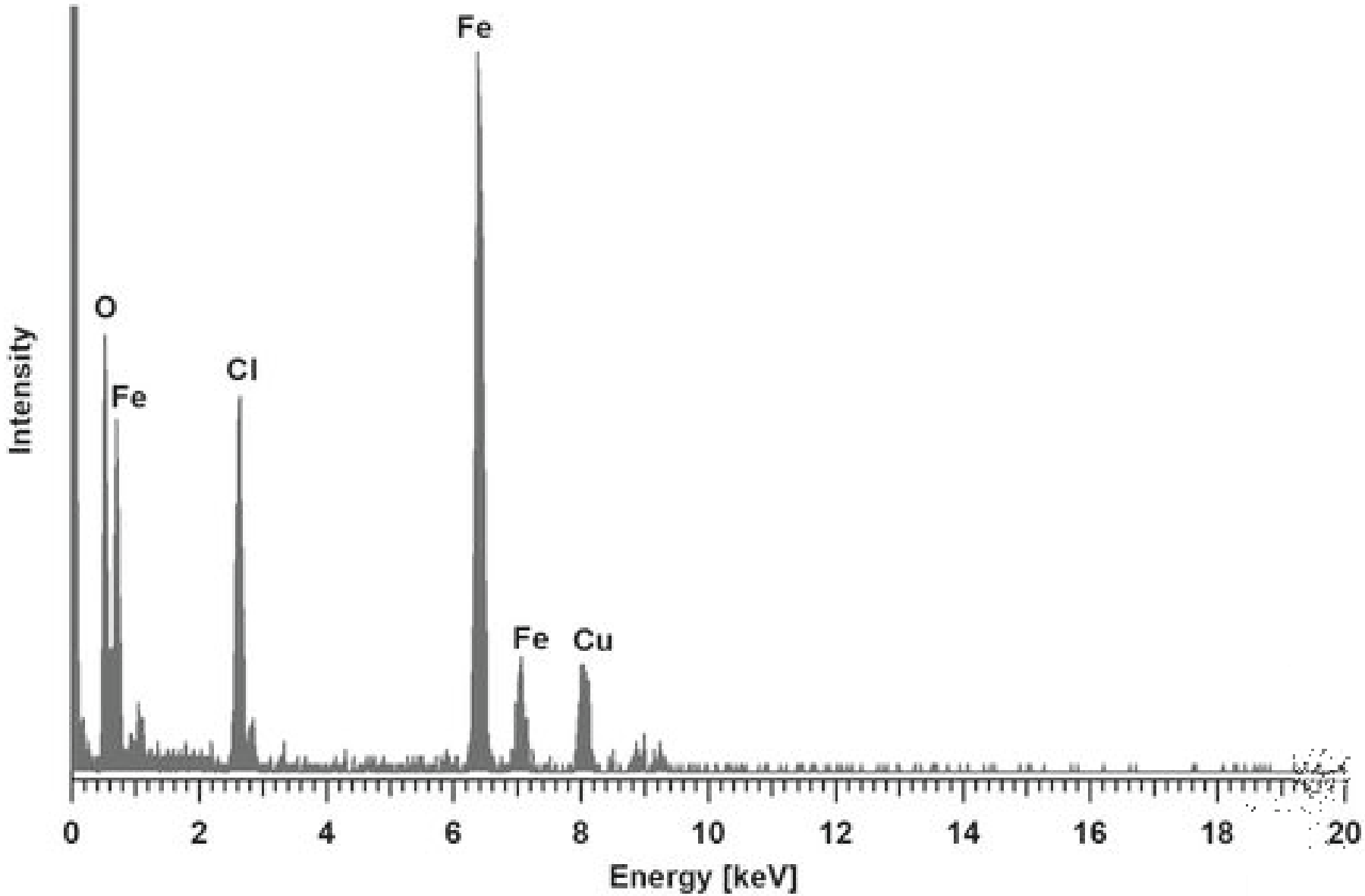

Figure 9